Monthly Notices
of the
ROYAL ASTRONOMICAL SOCIETY

Mon. Not. R. Astron. Soc. **416,** 155–177 (2011) doi:10.1111/j.1365-2966.2011.19018.x

Gemini/GMOS imaging of globular cluster systems in five early-type galaxies⋆

Favio R. Faifer,[1,2]† Juan C. Forte,[1] Mark A. Norris,[3] Terry Bridges,[4] Duncan A. Forbes,[5] Stephen E. Zepf,[6] Mike Beasley,[7] Karl Gebhardt,[8] David A. Hanes[9] and Ray M. Sharples[10]

[1]*Facultad de Cs. Astronómicas y Geofísicas, UNLP, Paseo del Bosque 1900, La Plata, and CONICET, Argentina*
[2]*Instituto de Astrofísica de La Plata (CCT La Plata - CONICET - UNLP), Argentina*
[3]*Department of Physics and Astronomy, University of North Carolina, Chapel Hill, USA*
[4]*Department of Physics, Engineering Physics, and Astronomy, Queen's University, Kingston, ON K7L 3N6, Canada*
[5]*Centre for Astrophysics and Supercomputing, Swinburne University, Hawthorn, VIC 3122, Australia*
[6]*Department of Physics and Astronomy, Michigan State University, East Lansing, MI 48824, USA*
[7]*Instituto de Astrofísica de Canarias, La Laguna 38200, Tenerife, Spain*
[8]*Astronomy Department, University of Texas, Austin, TX 78712, USA*
[9]*Department of Physics, Queen's University, Kingston, ON K7L 3N6, Canada*
[10]*Department of Physics, University of Durham, South Road, Durham DH1 3LE*

Accepted 2011 May 5. Received 2011 April 29; in original form 2010 December 17

ABSTRACT

In this paper, we present deep high-quality photometry of globular cluster systems (GCSs) belonging to five early-type galaxies, covering a range of mass and environment. Photometric data were obtained with the Gemini North and Gemini South telescopes in the filter passbands g', r' and i'. The combination of these filters with good seeing conditions allows an excellent separation between globular cluster (GC) candidates and unresolved field objects. In fact, our previously published spectroscopic data indicate a contamination level of only ∼10 per cent in our sample of GC candidates. Bimodal GC colour distributions are found in all five galaxies. Most of the GCSs appear bimodal even in the $(g' - r')$ versus $(r' - i')$ plane. A population of resolved/marginally resolved GC and ultracompact dwarf candidates was found in all the galaxies. A search for the so-called 'blue tilt' in the colour–magnitude diagrams reveals that NGC 4649 clearly shows this phenomenon, although no conclusive evidence was found for the other galaxies in the sample. This 'blue tilt' translates into a mass–metallicity relation given by $Z \propto M^{0.28\ \pm 0.03}$. This dependence was found using a new empirical $(g' - i')$ versus [Z/H] relation, which relies on an homogeneous sample of GC colours and metallicities. In this paper, we also explore the radial trends in both colour and surface density for the blue (metal-poor) and red (metal-rich) GC subpopulations. As usual, the red GCs show a steeper radial distribution than the blue GCs. Evidence of galactocentric colour gradients is found in some of the GCSs, which is more significant for the two S0 galaxies in the sample. Red GC subpopulations show similar colours and gradients to the galaxy halo stars in their inner region. A GC mean colour–galaxy luminosity relation, consistent with $[\ Z/H\ ] \propto L_B^{0.26\ \pm 0.08}$, is present for the red GCs. Estimates of the total GC populations and specific frequency S_N values are presented for NGC 3115, 3923 and 4649.

Key words: galaxies: elliptical and lenticular, cD – galaxies: star clusters: general.

⋆Based on observations obtained at the Gemini Observatory, which is operated by the Association of Universities for Research in Astronomy, Inc., under a cooperative agreement with the National Science Foundation (NSF) on behalf of the Gemini partnership: the NSF (United States), the Science and Technology Facilities Council (United Kingdom), the National Research Council (Canada), CONICYT (Chile), the Australian Research Council (Australia), Ministério da Ciência e Tecnologia (Brazil) and Ministerio de Ciencia, Tecnología e Innovación Productiva (Argentina).

†E-mail: favio@fcaglp.unlp.edu.ar

1 INTRODUCTION

The idea that globular clusters (GCs) are good tracers of very early events in the lives of galaxies was put forward many years ago (e.g. Eggen, Lynden Bell & Sandage 1962; Searle & Zinn 1978). A thorough description of all the important aspects is given, for example, in Brodie & Strader (2006). However, some key issues, such as the relation between GCs and galaxy field stars, still remain as open questions (see Kissler-Patig 2009). If such a relation does exist, some galaxy properties could be described in terms of the characteristics of their globular cluster systems (GCSs). A tentative approach in this direction (Forte, Faifer & Geisler 2007; Forte, Vega & Faifer 2009) assumes that GC formation efficiency depends on chemical abundance, and leads to a quantitative connection between field stars and GCs. In turn, this type of connection allows further analysis of the different GC–galaxy formation scenarios found in the literature (e.g. Ashman & Zepf 1992; Forbes, Brodie & Grillmair 1997; Beasley et al. 2002; Muratov & Gnedin 2010).

In this paper, we present new photometry for the GCSs of five early-type galaxies, using the imaging capabilities of the Gemini multi-object spectrograph (GMOS) instrument on the Gemini telescopes. This is part of a long-term study to obtain both imaging and spectra for these GCSs. Our first spectroscopic results were published for NGC 3379 (Pierce et al. 2006a), NGC 3923 (Norris et al. 2008) and NGC 4649 (Bridges et al. 2006; Pierce et al. 2006b). In particular, we aim at a detailed characterization of the most relevant photometric features of each GCS, such as colour bimodality, galactocentric colour gradients, spatial distributions and the presence (or absence) of the so-called 'blue tilt' in the colour–magnitude diagrams (CMDs) of the GCSs. All of these results will be analysed later in combination with the final spectroscopic sample. Additionally, a search for ultracompact dwarf (UCD) candidates was performed in each galaxy.

The paper is organized as follows. We describe the galaxy sample Section 2, and photometric observations and data handling in Section 3. In Section 4, we present the results in terms of CMDs and colour–colour diagrams, colour histograms, spatial distributions, galactocentric colour gradients and GC integrated luminosity functions. Finally, we give a summary in Section 5.

2 GALAXY SAMPLE

Our sample consists of five nearby early-type galaxies that cover a range of masses. These galaxies have been imaged in several filters over multiple pointings with the GMOS instrument on the Gemini telescopes. Basic data for the sample studied in this paper, ordered by decreasing luminosity (and presumably decreasing mass), are listed in Table 1. The sample comprises two S0 and three ellipticals (E), with B-band luminosities in the range $M_B = -19.94$ to -21.43. These are located in field (NGC 3115), group (NGC 3923, 524 and 3379) and cluster (NGC 4649) environments. In this work, we have adopted the distance modulus from the surface brightness fluctuation method presented by Tonry et al. (2001). This provides an homogeneous source, which can easily be converted to other distance scales, such as that of Jensen et al. (2003). In the following, we give a short description of each galaxy with references to earlier work pertaining to their GCS.

2.1 NGC 4649

Also known as M60, this Virgo cluster member is a giant elliptical (E2) within the Virgo cluster and is located in a subgroup to the east of the main cluster concentration. NGC 4647, a spiral some 2.5 arcmin to the north-west of NGC 4649, appears to be a background object as there is no evidence of reddening produced by this spiral on NGC 4649 (White, Keel & Conselice 2000) and no evidence of interaction between them. The GMOS fields presented here, and in our earlier work (Forbes et al. 2004), were chosen to minimize the effect of possible contamination of the NGC 4649 GCS by NGC 4647 GCs.

With a luminosity of $M_B = -21.43$, NGC 4649 is the most massive galaxy in our sample. Based on spectra of the central region, Terlevich & Forbes (2002) used Lick indices to measure an old age of 11 Gyr and a metallicity of [Fe/H] = 0.3. NGC 4649 shows strong X-ray emission arising from a hot gas halo (O'Sullivan, Forbes & Ponman 2001). *Chandra* observations reveal the presence of numerous discrete sources, which are mostly identified as low-mass binaries (LXMBs) within NGC 4649's GCs (Sarazin et al. 2003; Randall, Sarazin & Irwin 2004). Using the *XMM* satellite, Randall, Sarazin & Irwin (2006) present a hot gas density profile of slope -1.5 ± 0.1, determined between radii of 10 and 300 arcsec. Fukazawa et al. (2006) included this galaxy in their study of 53 ellipticals using archival *Chandra* X-ray data. Fitting a β model to the X-ray surface brightness profile, they obtained a value of $\beta = 0.512$, corresponding to a power-law slope of -2.07.

The NGC 4649 GCS was studied by Couture, Harris & Allwright (1991) in the B and V bands. Within the small CCD (2.1×3.4 arcmin) area, no bimodality was detected and the authors derived a mean colour of $(B - V) = 0.75$ based on 82 GC candidates.

Bimodality in the GC colour distribution was detected by Larsen et al. (2001) on the basis of *Hubble Space Telescope* (*HST*)/Wide Field and Planetary Camera 2 (WFPC2) observations, which found colour peaks at $(V - I)_0 = 0.95$ and 1.26. This bimodality was confirmed by Forbes et al. (2004) in the g' and i' bands using Gemini/GMOS imaging. These authors estimated a total GC

Table 1. Galaxy sample. Coordinates and Hubble types are taken from the NED, B magnitudes are from the RC3 catalogue (de Vaucouleurs et al. 1991), the distance modulus is from Tonry et al. (2001), the extinction is from Schlegel et al. (1998) and the X-ray luminosity is from O'Sullivan et al. (2001).

Galaxy	α_{J2000} (h:m:s)	δ_{J2000} (°:′ : ″)	l (°:′ : ″)	b (°:′ : ″)	Type	B_T^0 (mag)	M_B (mag)	A_B (mag)	$(m-M)_0$ (mag)	$\log L_X$ (erg s^{-1})	Environ.
NGC 4649	12:43:39.7	+11:33:09.4	295:52:10.2	+74:19:3.36	E2	9.70	−21.43	0.116	31.13 ± 0.15	41.28	Cluster
NGC 3923	11:51:01.8	−28:48:22.0	287:16:34.0	+32:13:21.4	E4-5	10.62	−21.18	0.362	31.80 ± 0.28	40.66	Group
NGC 524	01:24:47.7	+09:32:20.0	136:30:20.2	−52:27:05.4	S0	11.17	−20.73	0.362	31.90 ± 0.20	40.53	Group
NGC 3115	10:05:14.1	−07:43:07.0	247:46:58.8	+36:46:53.0	S0	9.74	−20.19	0.207	29.93 ± 0.09	39.72	Field
NGC 3379	10:47:49.6	+12:34:54.0	233:29:24.7	+57:37:58.4	E1	10.18	−19.94	0.107	30.12 ± 0.11	< 39.52	Group
CF	22:37:24.2	+22:48:20.5	86:44:10.8	−30:29:07.5							
WHDF	00:22:32.8	+00:21:07.5	107:34:49.5	−61:39:20.7							

population of 3700 ± 900, giving a specific frequency $S_N = 4.1 \pm 1$. These values are in good agreement with those presented by Lee et al. (2008) in their Washington CT_1 photometric study. Pierce et al. (2006b) found that most of their 38 spectroscopically confirmed GCs are old (>10 Gyr), but they found some young and super-solar metallicity GCs. This sample was used by Bridges et al. (2006) to analyse the GC kinematics and dark matter content of NGC 4649 within 3.5 effective radii (20 kpc). No rotation of the GCS was detected, and both isotropic and axisymmetric orbit-based models gave support for the presence of a dark matter halo in NGC 4649.

2.2 NGC 3923

This is an E4–5 galaxy within a small group and it exhibits a well-known shell structure (Malin & Carter 1980). This type of structure is frequent in ellipticals and S0 galaxies not belonging to galaxy clusters (Schweizer & Seitzer 1992). It is usually identified as the result of an interaction or merger (e.g. Quinn 1984; Thomson & Wright 1990). These shell structures may be long-lived and therefore an interaction/merger event may have occurred a long time ago.

From spectroscopic data, Thomas et al. (2005) and Denicoló et al. (2005) derive central galaxy ages of 3.4 and 2.6 Gyr, respectively. Thus, about 3 Gyr ago, the galaxy appears to have experienced a central starburst (perhaps induced by the same event that created the shells). The galaxy has a halo of hot gas (e.g. O'Sullivan et al. 2001). Using the *ROSAT* satellite, Buote & Canizares (1999) fit a β model to the X-ray surface density profile out to 500 arcsec. They derived a power-law slope of -1.76 ± 0.02. Fukazawa et al. (2006) fitted a double β model to the X-ray surface brightness and found β values of 0.598/0.314 for the less/more extended component. These values correspond to power-law slopes of $-2.54/-0.88$.

Two previous photometric studies (Zepf, Geisler & Ashman 1994; Zepf, Ashman & Geisler 1995), using ground-based Washington C and T_1 photometry, noted the presence of colour peaks at $(C - T_1) = 1.47$ and 1.87, somewhat redder than typical values. This led these authors to suggest a higher than average metal content for the NGC 3923 GCs. The total GC population was estimated to range from 2000 to 7000, and the S_N from 4.4 to 7.3. More recently, using *HST*/Advanced Camera for Surveys (ACS) imaging, Sikkema et al. (2006) measured similar blue and red GC projected density slopes of -0.87. However, their fits were obtained within the central 100 arcsec and could be affected by the flattening of the inner GC profiles, as seen in many other galaxies. They obtained an S_N value of 5.6, and concluded that NGC 3923 has the highest S_N of any isolated elliptical.

Norris et al. (2008) have found that the GCs spectroscopically examined are old (>10 Gyr) with [Z/H] $= -1.8$ to 0.35. Additionally, they have shown that the diffuse light of the galaxy at $3R_e$ is found to have ages, metallicities and [α/Fe] abundance ratios indistinguishable from those of the red GCs.

There are two spectroscopically confirmed UCDs in this galaxy, found by Norris & Kannappan (2011).

2.3 NGC 524

This galaxy is part of a group, known as CfA 13, which includes at least eight smaller galaxies (Geller & Huchra 1983). This group was detected in the X-ray study by Mulchaey et al. (2003). The β parameter fitted to this galaxy is 0.41 ± 0.02, which translates into a power-law slope of -1.46 ± 0.12. The galaxy nucleus appears to be chemically decoupled from its bulge, being about 0.5–0.6 dex more metal-rich according to Sil'chenko, Afanasiev & Vlasyuk (1992) and Sil'chenko (2000), who also find evidence for a dusty disc and ionized gas within 3 kpc of the galaxy centre.

Harris & Hanes (1985) found a rich and extended GCS with some 2830 ± 880 clusters. Larsen et al. (2001) used a KMM analysis on *HST*/WFPC2 data to find colour peaks at $(V - I)_0 = 0.98$ and 1.19 mag. More recently, Beasley et al. (2004) found a broad $(V - I)$ colour distribution and the possible existence of peaks at $(V - I)_0 = 0.9$ and 1.1. However, none of these results is conclusive. The Keck/LRIS spectra from Beasley et al. of a small sample of GCs point to a metallicity range from [Fe/H] $= -2.0$ to 0.0 and a decreasing trend of the [α/Fe] ratio with metallicity. The GCs are generally consistent with being old. Regarding UCDs, there is one confirmed object by Norris & Kannappan (private communication).

2.4 NGC 3115

This is a relatively isolated S0 galaxy with a dominant bulge, located to the south of the Leo group. The X-ray emission from NGC 3115 is low, contained within 10 kpc, and probably dominated by discrete sources (Fukazawa et al. 2006). Its GCS is bimodal with colour peaks at $(V - I)_0 = 0.96$ and 1.17, and it has a low local S_N value of $\sim$1.3 within the inner region of the galaxy (Kundu & Whitmore 1998). These authors also find that while the red GC subpopulation has a spatial distribution comparable to that of the thick disc, the blue GCs exhibit a distribution more similar to the bulge/halo.

Selecting from the Kundu & Whitmore (1998) GC sample, Kuntschner et al. (2002) derived spectroscopic ages and metallicities for 17 GCs, finding both subpopulations to be $\sim$12 Gyr old and coeval within 2–3 Gyr. This result is consistent with Puzia et al. (2002), who also find coeval ages within 3 Gyr.

From GMOS spectroscopy of the galaxy halo, Norris, Sharples & Kuntschner (2006) calculated an age of 10–12 Gyr, similar to that of the GCs. They also obtain an [α/Fe] ratio of $\sim$0.2–0.3, consistent with the typical GC values.

2.5 NGC 3379

This galaxy is the dominant object of the nearby Leo group. Terlevich & Forbes (2002) derive an old central age of $\sim$9.3 Gyr, consistent with ages larger than 8 Gyr determined using *HST*/Near-Infrared Camera and Multi-Object Spectrometer (NICMOS) observations of resolved stars by Gregg et al. (2004). The galaxy contains a very modest hot gas halo, and Revnivtsev et al. (2008) suggest that a significant contribution to the observed X-ray flux of the galaxy comes from unresolved point sources.

From a CCD study of the NGC 3379 GCS, Ajhar & Tonry (1994) detected $\sim$60 GCs but no evidence of bimodality. Using *HST*/WFPC2, Larsen et al. (2001) have confirmed that NGC 3379 contains a poor GCS. Both Whitlock, Forbes & Beasley (2003) and Rhode & Zepf (2004) found evidence of bimodality using broad-band colours. Rhode & Zepf (2004) estimated a total GC population of 270 clusters, giving a low S_N value of 1.2 ± 0.3.

In their spectroscopic study, Pierce et al. (2006a) found the GCs to be consistent with old ages (i.e. 10 Gyr), with a wide range of metallicities.

Table 2. Summary of observations. This table lists the programme ID, the numbers of the fields, the exposures and the final seeing of the co-added images.

Galaxy	Gemini ID	Fields	$T_{\rm exp.}$ (s) g' r' i'	FWHM (arcsec) g' r' i'
NGC 4649	GN-2007A-Q-37	1	4 × 120 4 × 120 4 × 120	0.48 0.49 0.48
		2	4 × 120 4 × 120 4 × 120	0.48 0.45 0.45
	GS-2007A-Q-49	3	4 × 120 4 × 120 4 × 120	1.11 1.05 1.12
	GN-2007A-Q-37	4	4 × 120 4 × 120 4 × 120	0.51 0.51 0.47
NGC 524	GN-2002B-Q-25	1	4 × 150 4 × 100 4 × 100	0.67 0.60 0.65
		2	6 × 150 4 × 100 5 × 100	0.85 0.76 0.72
		3	4 × 100 4 × 100 5 × 100	0.79 0.81 0.84
NGC 3379	GN-2003A-Q-22	1	4 × 200 4 × 100 4 × 100	1.03 0.99 0.84
		2	4 × 200 4 × 100 4 × 100	0.54 0.54 0.52
		3	4 × 200 4 × 100 4 × 100	0.93 0.98 0.90
NGC 3115	GS-2004A-Q-9	1	4 × 200 4 × 100 4 × 100	0.77 0.65 0.53
		2	4 × 200 4 × 100 4 × 100	0.80 0.84 0.70
NGC 3923	GS-2004A-Q-9	1	4 × 200 4 × 100 4 × 100	0.79 0.68 0.67
		2	4 × 200 4 × 100 4 × 100	0.72 0.62 0.55
		3	4 × 200 4 × 100 4 × 100	0.72 0.63 0.59
CF	GN-2003A-Q-22	1	3 × 200 3 × 100 3 × 100	0.64 0.55 0.50
WHDF	GN-2001B-SV-104	1	6 × 300 6 × 300 6 × 300	0.86 0.67 0.67
Blank-sky	GS-CAL20040120	1	7 × 300	0.47

3 DATA

3.1 Observations and data reduction

The images presented here were taken using GMOS (Hook et al. 2004)[1] in imaging mode on both the Gemini South and Gemini North telescopes. The instruments consist of three 2048 × 4608 pixel CCDs, with a scale of 0.0727 arcsec pixel^{-1}. We used 2 × 2 binning, yielding a 0.146 arcsec pixel^{-1} scale. The GMOS camera has a field of view of 5.5 × 5.5 arcmin^2. Except for NGC 524 and our comparison field (CF), where we had to reject and repeat some bad images, four images per field were taken for each of the three SDSS filters, g', r' and i' (Fukugita et al. 1996). The telescope was dithered between exposures to facilitate cosmic-ray removal and to fill the gaps between the CCD chips. Details of the observational parameters are given in Table 2. In addition, we make use of the William Herschel Deep Field (WHDF) to help estimate contamination (see Section 3.4). Fig. 1 shows the positions of the GMOS fields around each galaxy superimposed on Digital Sky Survey (DSS) images.

With the aim of obtaining an homogeneous photometric sample, we rereduced the images provided by Gemini. The raw images were processed using the Gemini GMOS package within IRAF[2] (GPREPARE, GBIAS, GIFLAT, GIREDUCE, GMOSAIC). In all cases, we chose suitable sets of raw bias and flat-field frames from the available data in the Gemini Science Archive (GSA). The images taken with the i'-band filter on Gemini South show considerable fringing. We therefore built suitable fringe images from seven exposures of blank-sky regions taken as part of the baseline calibration the night after the observations of NGC 3923 and 3115. These frames were used to correct i' images (listed in Table 2) by means of the GIFRINGE and GIRMFRINGE tasks. The resulting images for each filter were then co-added and cosmic-ray cleaned using IMCOADD. Because the images were taken in queue mode, some were obtained under slightly different sky conditions. As a consequence, we set 'fl_scale = yes' in order to combine images with different FWHM and signal. In this step, we tuned some IMCOADD parameters, such as 'aperture' and 'statsec', and we set 'scalenoise ∼3', in order to avoid losing good pixels and spurious zero-point offsets during the adding process. These final co-added images were then used for all the subsequent data analysis.

3.2 Photometry

Galaxy light subtraction was performed using an iterative combination of the SEXTRACTOR background modelling approach (Bertin & Arnouts 1996) and median filtering, in a similar way to that presented in Puzia et al. (2004). This procedure was implemented in a script, which yields a catalogue of all the objects detected by SEXTRACTOR and a galaxy light subtracted image. This software gives better results than IRAF tasks such as DAOFIND. As in Forbes et al. (2004), the list of i'-band objects was adopted as input for the subsequent photometry. At the distance of the targets listed in Table 1, most of the GCs would be expected to be unresolved (star-like) sources. The DAOPHOT package (Stetson 1987) within IRAF was used to obtain point spread function (PSF) magnitudes for all objects detected by SEXTRACTOR. These were then separated into resolved and unresolved objects, following the outline presented in Section 3.3. After this, aperture photometry was obtained for all the resolved objects. For this purpose, we have used the PHOT task with a fixed 2-arcsec aperture. This means that we have good photometry for unresolved and marginally resolved objects. A 'master' catalogue of resolved and unresolved objects was built by combining photometry of objects successfully measured in all three filters.

We searched in the GSA for standard star fields observed during the same nights as our targets and the CF. These were rereduced using the same biases and flats applied to our science frames. The synthetic transformation from Fukugita et al. (1996) was adopted to obtain the g', r' and i' standard magnitudes. Because of the small number of the available standards, usually three to four stars, and

[1] Further information on GMOS can be found on the instrument homepage (http://www.gemini.edu/sciops/instruments/gmos/).

[2] IRAF is distributed by the National Optical Astronomical Observatories, which are operated by the Association of Universities for Research in Astronomy, Inc., under cooperative agreement with the NSF.

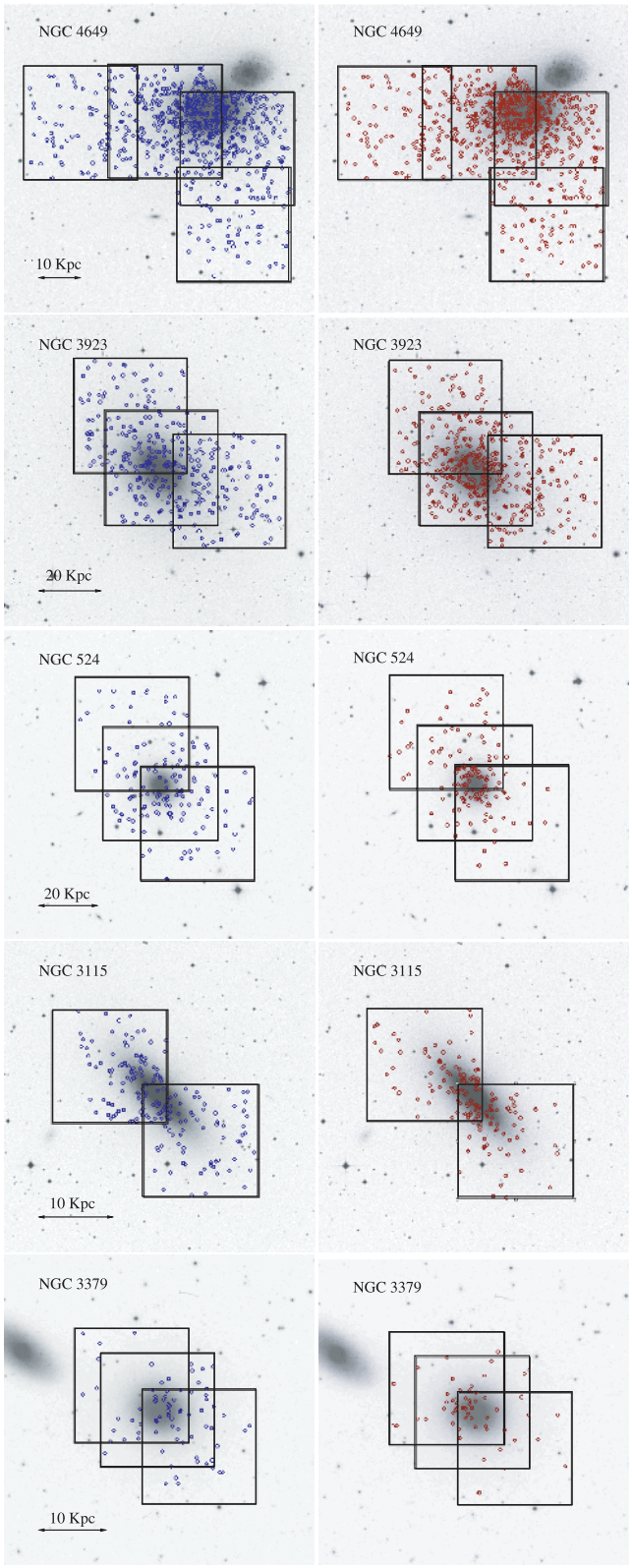

Figure 1. *R*-band images of the sample galaxies from the DSS2. Each image has a field of view of 15 × 15 arcmin^2. From top to bottom, we show NGC 4649, 3923, 524, 3115 and 3379. For each galaxy, we display the red GC candidates in the right panels, and the blue GC candidates in the left panels. The GMOS fields are also depicted. North is up and east is to the left.

their very limited range in airmass, this calibration was suitable only for establishing a mean zero-point value for our frames, and not for a more complete evaluation of the coefficients in airmass or colour (see Table 3). Thus, we measured these zero-points, and we used the atmospheric extinction coefficients given by the Gemini web page.

NGC 4649 is an exception because standards were not observed at the same night as our programme fields. So, in this case, we adopted the mean zero-points obtained from the three sets of standards (about five stars per field) observed during the Gemini North GMOS run of 2007 March.

For each galaxy, the field with the best overall seeing in the three filters, and having a corresponding standard star field, was adopted as the reference for the photometry. A list of common objects in each field was used to obtain any small zero-point differences among the pointings. Finally, we applied the galactic extinction coefficients given by Schlegel, Finkbeiner & Davis (1998), and we used their table 6 to transform these into $A_{g'}$, $A_{r'}$ and $A_{i'}$. Thus, we quote extinction-corrected magnitudes and colours in this paper.

3.3 Object classification and completeness

The classification between resolved and unresolved sources was carried out using the same procedure as in Forbes et al. (2004). Briefly, we used a combination of SEXTRACTOR stellarity index (0 for resolved objects and 1 for unresolved objects), and the positions of each object in the aperture minus PSF magnitude versus PSF magnitude diagram (Forte et al. 2001; see also figs 1 and 2 from Forbes et al. 2004). This approach has been tested using our follow-up spectroscopic studies (Bridges et al. 2006; Pierce et al. 2006a; Norris et al. 2008). Combined with three-colour selection, this has been very successful in giving a low contamination rate by background galaxies.

In order to quantify the detection limits of our photometry, a series of completeness tests was carried out on each field using the ADDSTARS task. The i'-band magnitude range from 18.5 to 26.5 mag was divided into intervals of 0.1 mag. Then, trying to avoid crowding effects, 200 point sources were added to the original i' images in each magnitude bin. The same procedure of galaxy light subtraction, detection and classification was followed to recover and classify the added sources. The positions of the artificial objects were created using a stochastic-generating FORTRAN program, which follows the slope of the GCS spatial distribution. A total of 32 000 artificial objects were added in two independent experiments per field.

As an example, Fig. 2 shows a typical result of this procedure. In this case, we plot the results for each of the i' fields of NGC 3923. The left panel shows the fraction of artificial objects recovered versus the input magnitude for each field. The right panel shows the completeness as a function of $R_{\rm gal}$ for three different magnitude bins in field 1. If a global completeness level is selected from the left plot, the right panel shows that most of the objects are lost at small $R_{\rm gal}$. That is, the completeness has a strong spatial dependence in the sense that the loss of objects is always larger at small radii. Taking this into account, and in order to ensure completeness levels greater than 50 and 90 per cent for $R_{\rm gal} > 45$ arcsec, we selected the i'-band limits listed in Table 3. The 50 per cent level was used to define a sample of GC candidates, but we used the 90 per cent level in the subsequent analysis.

3.4 Comparison fields

In addition to the galaxy sample listed in Table 1, we include two CFs. One of these is the same as in Forbes et al. (2004).

Table 3. Ranges adopted for GC candidate selections, zero-points and completeness levels in the i'_0 band.

Galaxy	i'_0	$(g'-i')_0$	$(g'-r')_0$	$(r'-i')_0$	$Z_p\,g'$	$Z_p\,r'$	$Z_p\,i'$	Completeness	
								90 per cent	50 per cent
NGC 4649	19.5–24.3	0.40–1.45	0.35–0.95	0.0–0.60	27.885 ± 0.005	28.268 ± 0.004	28.190 ± 0.006	23.90	24.30
NGC 3923	20.0–23.7	0.40–1.40	0.30–0.90	0.0–0.60	28.239 ± 0.006	28.128 ± 0.008	27.711 ± 0.009	23.30	23.70
NGC 524	20.4–23.5	0.40–1.40	0.30–0.90	0.0–0.60	27.630 ± 0.018	27.992 ± 0.028	27.777 ± 0.030	23.00	23.50
NGC 3115	18.4–23.5	0.40–1.40	0.30–0.90	0.0–0.60	28.239 ± 0.006	28.128 ± 0.008	27.711 ± 0.009	23.00	23.50
NGC 3379	18.6–23.2	0.40–1.40	0.30–0.90	0.0–0.60	27.985 ± 0.006	28.215 ± 0.005	27.961 ± 0.004	22.90	23.20
CF					27.905 ± 0.017	28.189 ± 0.028	27.977 ± 0.017	24.00	24.33
WHDF					27.934 ± 0.020	28.184 ± 0.029	27.942 ± 0.030	24.75	25.05

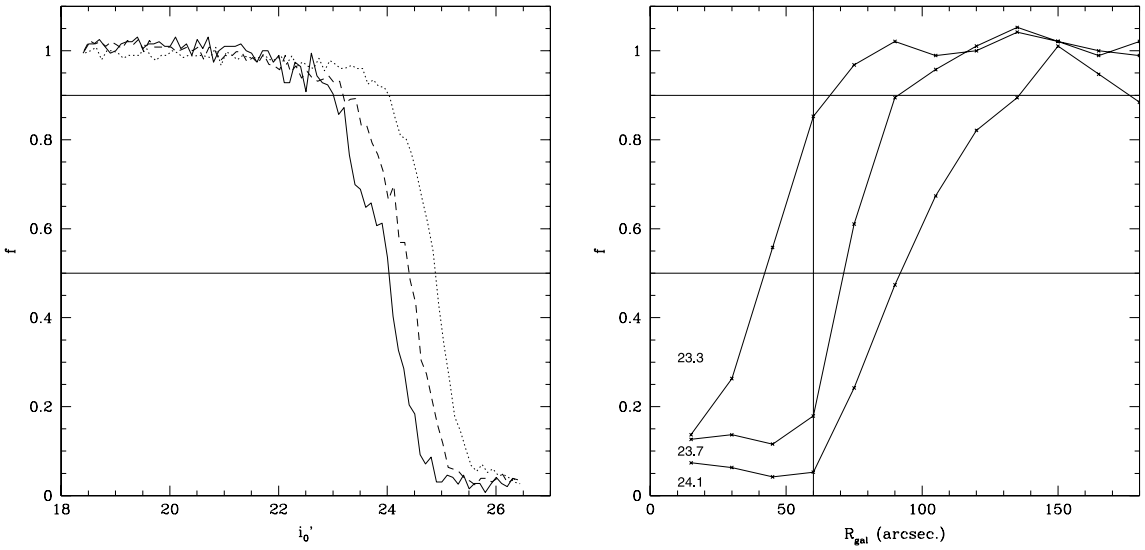

Figure 2. Completeness factors for the *i* images of NGC 3923. The solid, dotted and dashed lines correspond to fields 1, 2 and 3, respectively. Left panel: fraction of recovered objects versus the input magnitudes. Field 1 (centred in the galaxy) shows a smaller overall completeness than fields 2 and 3. The solid lines are the 90 and 50 per cent levels. Right panel: completeness for field 1 versus galactocentric radius for three different magnitude bins. The fraction of lost objects is strongly dependent on galactocentric radius for $R < 100$ arcsec.

However, here we present rereduced and recalibrated data for this field.

We have applied the same object detection and classification procedures as for our programme images. Fig. 3 shows, in the upper panel, the CMDs for the unresolved and resolved objects in this field. For unresolved objects, we used PSF magnitudes, while for resolved objects we used aperture photometry with 2-arcsec apertures. Most of the objects with magnitudes $i'_0 < 23.5$ and colours within the ranges adopted for GC candidates are resolved and have been correctly classified (see Section 4.1). However, for $i'_0 \sim 23.5$, the situation is very different and there are many point sources displaying $(g' - i')$ colours similar to those of GCs. Most of these are probably distant background galaxies.

In order to test the results obtained with our CF, we applied our classification recipe on the WHDF (Metcalfe et al. 2001). This field was observed with the same instrument and filters as our CF. The seeing in both fields is similar, so the only differences are the total exposure times (see Table 2). The 90 and 50 per cent completeness levels obtained for our CF and the WHDF are listed in Table 3.

Fig. 3 shows, in the bottom panel, the CMDs for unresolved and resolved objects detected in the WHDF. Clearly, there are two main differences between the two CMDs in Fig. 3. First, there are different numbers of star-like objects brighter than $i'_0 < 23.5$ present in these fields. There are more stars in our CF than in the WHDF. This is easily seen in the red side of the CMD of the unresolved objects $[(g' - i') > 1.5]$.

The other difference is the appearance of the CMD at the low-brightness extreme. The number of unresolved objects in the CF drops steeply at $i'_0 \sim 23.5$, whereas in the WHDF this does not occur until $i'_0 \sim 24.2$. The reason for this behaviour is that the process of classification improves with better signal-to-noise ratio (S/N) – i.e. with the deeper WHDF exposures, we can make a better classification – and that the stellar content is not the same in both fields, as expected given their different galactic latitudes. However, we note that the number of stars with colours adopted here for GC candidates is only 30 per cent larger in the CF than in the WHDF. Comparing the star counts in this field with the number from the Besancon galaxy models (Robin et al. 2003), we found a very good agreement for $i'_0 < 23.5$. For fainter magnitudes, the Besancon star counts are always smaller than the observed counts, possibly indicating a very strong contamination by unresolved background galaxies.

The analysis given in Fukugita, Shimasaku & Ichikawa (1995) suggests that low-redshift S, S0 and E galaxies and medium-redshift Irr galaxies can show colours in the ranges adopted for the GC candidates. However, under good imaging conditions (i.e. subarcsecond FWHM) and making a careful image analysis, most of these are

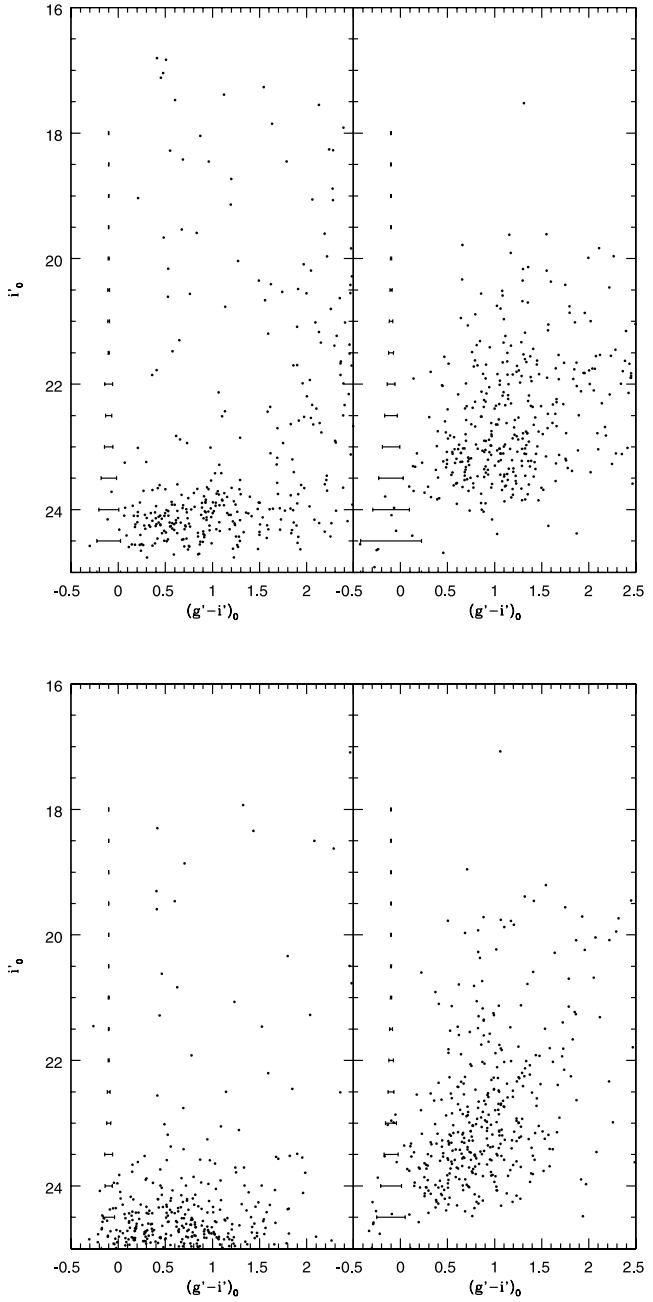

Figure 3. Photometric properties of the sources detected in our CF (top panel) and in the WHDF (lower panel). In each panel, the left/right plot shows the CMD for unresolved/resolved sources. Mean colour errors are shown by the horizontal bars in each panel. It is possible to efficiently separate background galaxies from MW stars only for objects brighter than $i'_0 \sim 23.5$.

correctly classified as extended sources. The medium- and high-redshift galaxies are difficult to resolve from ground-based observations. However, most of these objects can be rejected by using $(g' - i')$, $(g' - r')$ and $(r' - i')$ colours.

This means that, for $i'_0 < 23.5$, the nature of the contamination is mainly stellar. At fainter magnitudes, the contamination arising from faint background galaxies increases steeply.

In the subsequent analysis, we adopt an average of the counts in both fields to obtain the contamination levels of our photometry in NGC 3923, 524, 3115 and 3379. In the case of NGC 4649, we chose to use only the WHDF as a CF for two reasons. The first reason is that the photometry in the CF is not deep enough. The second reason is that, as we see in Section 4, the CMDs of the objects detected in our four NGC 4649 fields show a very small number of objects outside the regions occupied by GC candidates. The main difference between the WHDF and our CF is the red side of the colour distribution.

4 RESULTS

4.1 Colour–magnitude and colour–colour diagrams

The CMDs and colour–colour diagrams are presented in Fig. 4 for all point sources detected in our GMOS fields (small dots), ordered by decreasing B_T brightness of the host galaxy. Magnitudes and colours were corrected for galactic extinction, as indicated in Section 3.2. The mean $(g' - i')$ photometric errors are shown as small bars at $(g' - i')_0 = 0$. The dotted and long-dashed lines indicate the 50 and 90 per cent completeness limits from our completeness tests, respectively.

In all diagrams, the GCs can be easily seen as a group of objects clustered around $(g' - i')_0 \sim 0.8$, $(g' - r')_0 \sim 0.6$ and $(r' - i')_0 \sim 0.3$. In order to obtain a clean sample of GC candidates, rejecting Milky Way (MW) stars and unresolved background galaxies, but allowing a reasonable range of GC colours, we adopted the limits listed in Table 3. Regarding the magnitude limits, cuts were applied only on the i'-band magnitudes. The low-brightness ends were defined by the 50 per cent completeness level in the case of our photometric sample definition, and by the 90 per cent completeness level for the analysis sample (which was used in the analysis presented in the following sections).

For the high-brightness end, the cuts were chosen in order to include all GC candidates with absolute magnitudes fainter than $M_I \approx -12$. The most massive galactic GC-like object, ω Cen, has an integrated magnitude of $M_I \sim -11$. However, M31's most massive GC, G1, is considerably more luminous. Also, this upper limit is in agreement with the $M_V = -11$ value suggested by Mieske et al. (2006a) to separate bright GCs from UCDs, and it is similar to that found by Wehner & Harris (2007) for the Hydra UCD candidates. Adopting this upper limit, and utilizing common objects between our GMOS photometry and that of Larsen et al. (2001) from *HST* data, we obtain the $(g', i') - (V, I)$ transformations:

$$I_0 = i'_0 - 0.491(\pm 0.003); \quad (1)$$

$$V_0 = g'_0 - 0.34(\pm 0.02)(g' - i')_0 - 0.03(\pm 0.02); \quad (2)$$

$$(V - I)_0 = 0.80(\pm 0.02)(g' - i')_0 + 0.32(\pm 0.02). \quad (3)$$

Taking into account the distance modulus from Table 1, we obtain the upper cut values listed in Table 3, which roughly correspond to $M_I = -12$ in each galaxy. Fig. 4 shows as filled circles all the point sources falling in the colour and magnitude ranges listed in Table 3, which we take as our GC candidates.

Most of the unresolved objects in our sample define clear sequences consistent with the locus of MW stars. The more sparse appearance of the colour diagrams corresponding to NGC 524 is probably because of the slightly lower quality of the photometry. In the case of NGC 4649, we have higher quality and deeper photometry. The 50 per cent completeness level is fainter than that in any other galaxy. Therefore, we expect a slightly higher level of contamination by faint background objects (as shown in Section 3.4, the number of background objects grows steeply for $i'_0 > 23.5$).

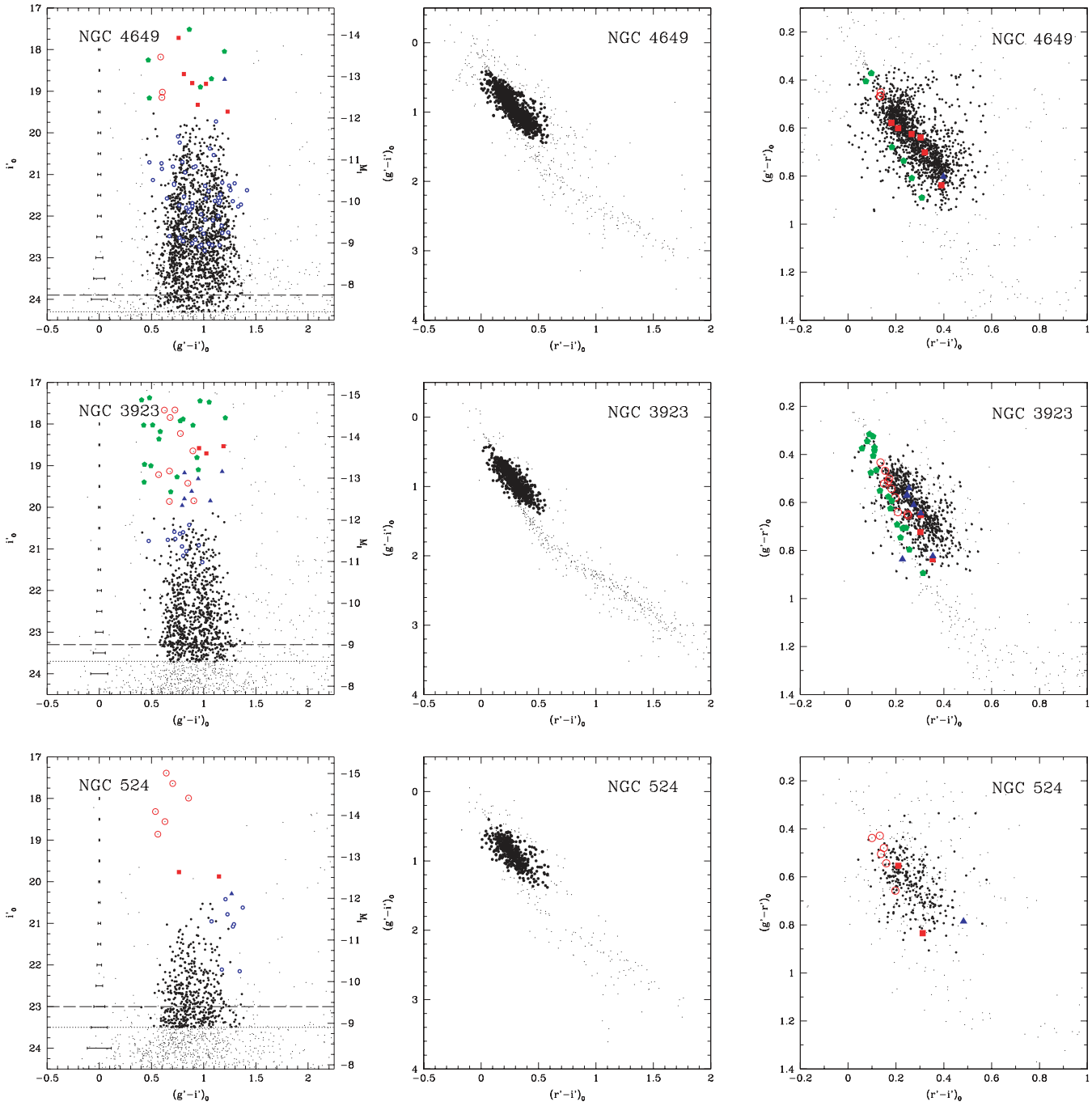

Figure 4. CMDs and colour–colour diagrams for all the point sources detected in our GMOS fields (small dots). The dotted and long-dashed lines indicate the 50 and 90 per cent completeness levels, respectively. The mean errors in $(g' - i')$ are plotted as small bars in the CMDs. Big dots are our GC candidates selected as indicated in the text. In the CMDs and in the $(g' - r')$ versus $(r' - i')$ diagrams, we show the UCD candidates: type I (red filled squares), type II (red circles) and type III (green pentagons). The marginally resolved GCs are plotted as big blue circles and the resolved UCDs as blue filled triangles.

In both colour–colour diagrams, the GC candidates form a short sequence, which merges with MW stars in the blue extreme. Thus, a small fraction of the candidates with extreme colours, $(g' - i')_0 \sim 0.5$, could in fact be Galactic stars.

As mentioned before, at the distances of the targets listed in Table 1 we can expect that the normal GCs will look like unresolved objects. However, in the cases of NGC 4649 and 3923, Bridges et al. (2006) and Norris et al. (2011) have found marginally resolved objects with colours similar to blue GCs, which were confirmed as members of the NGC 4649 and 3923 GCSs. Considering that most of the images in Table 3 were taken with subarcsecond image quality, and because two of our targets are relatively nearby systems, we have checked the possibility that other marginally resolved GC-like objects exist in the lists of extended sources. Therefore, we inspected by eye all objects classified as resolved, but having SEXTRACTOR shape parameters, indicating roundness similar to that of

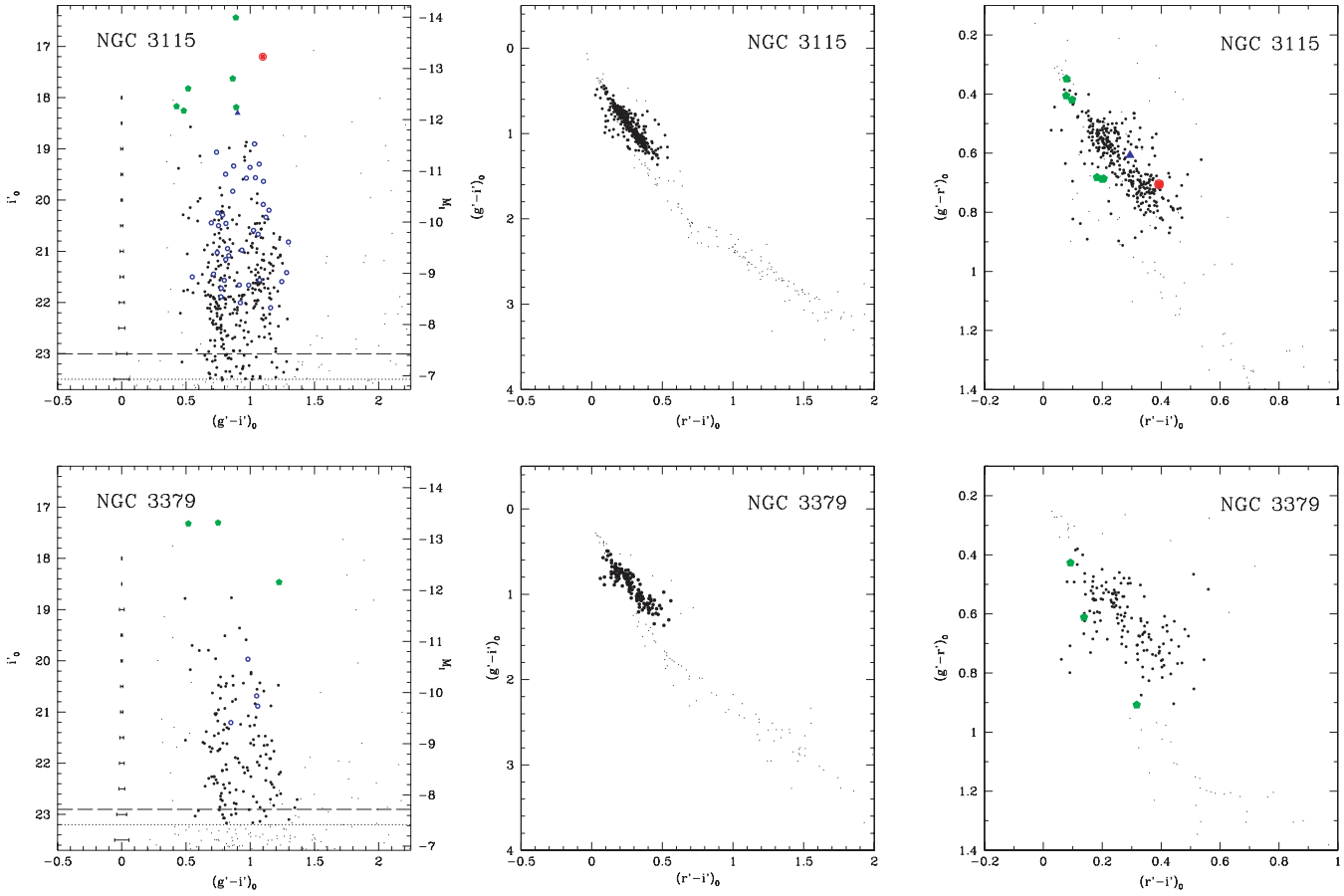

Figure 4 – *continued*

point sources in each image. As noted in Section 3.3, a good S/N is necessary to robustly determine these parameters; therefore, we only analysed objects brighter than $i'_0 = 22$–23 mag. Any object showing a complex structure was rejected and aperture photometry was performed on the remaining sources. These are indicated as blue open circles in the CMDs, and with the same symbols as GC candidates in the colour–colour diagrams. This sample of marginally resolved objects is expected to have a higher level of contamination by background galaxies than our final sample of GC candidates.

Because the half-light radii of UCD candidates (5–100 pc, according to Mieske et al. 2008) are larger than those typical for GCs, we have extended the inspection described in the last paragraph to higher luminosities, including both unresolved and marginally resolved sources. Plotting the point-source UCD candidates in the colour–colour diagrams – see the $(g' - r')$ versus $(r' - i')$ panels for NGC 4649 and 3923 in Fig. 4 – they seem to define two distinct groups. One group includes objects falling exactly on the GC sequence. The other group falls on the MW stellar sequence, which merges with that of the GCs at the blue extreme. Considering this, we have classified our unresolved UCD candidates as follows: 'type I', if they belong to the first group (the most secure, shown as red filled squares in Fig. 4); 'type III', if they belong to the second group (less secure, and probably MW stars, shown as green filled pentagons in Fig. 4). Additionally, we have defined 'type II' as those objects that seem to overlap both groups (red circles in Fig. 4). Some marginally resolved UCD candidates, shown as blue filled triangles in Fig. 4, were also found. The full photometric tables are presented in Appendix A. Here, we give a summary of each GCS.

4.1.1 NGC 4649

This galaxy shows a well-defined GC sequence in the colour–colour diagram. The bimodality in $(g' - i)$ is clear and detectable even in the $(g' - r')$ versus $(r' - i')$ plane, where we can see two slightly superimposed clumps of GCs. There are bright blue and red GC candidates ($M_I < -11$), so the brightest objects suggest a non-unimodal colour distribution. However, the most striking characteristic in NGC 4649 is that the bluest GCs seems to become redder with increasing luminosity (i.e. they show a 'blue tilt', as discussed later).

We have found 63 marginally resolved GC candidates (shown as blue circles), some of which were confirmed as belonging to the NGC 4649 system by Bridges et al. (2006) (see Table A1). These objects have a broad colour distribution but they seem to follow that of the GCs.

Regarding UCD candidates, we have found 15 unresolved objects and one marginally resolved bright object. All of these have absolute magnitudes $-14.5 < M_I < -12$, well in the UCD luminosity range. We have six type I UCD candidates (including the one marginally resolved), three type II and six type III.

4.1.2 NGC 3923

The GC bimodality is easily detectable, but only for objects with $M_I > -11$. In contrast with NGC 4649, the brightest objects show a broad and nearly unimodal distribution. This phenomenon has previously been observed in other giant galaxies,

such as NGC 1399 (Ostrov, Forte & Geisler 1998; Dirsch et al. 2003).

In this galaxy, we find 12 marginally resolved objects, all with blue colours: $(g' - i')_0 < 1.0$. A few have been confirmed by Norris et al. (2011) as members of the NGC 3923 system. In particular, object ID 285 is a clearly extended object. We have also found 32 unresolved objects with $-15 < M_I < -12$, (three type I and 10 type II). The remaining 19 type III UCD candidates are very probably MW stars. One of our type I candidates, ID 336, was spectroscopically confirmed by Norris & Kannappan (2011) as a real UCD (UCD1 in their table 3). Regarding marginally resolved UCD candidates, we have found seven, a relatively large number. Two of these, ID 760 and ID 1030, were confirmed as members of the NGC 3923 system by Norris et al. (2011) and ID 243 was confirmed by Norris & Kannappan (2011) (UCD2 in their table 3).

4.1.3 NGC 524

This galaxy shows a broad GC colour distribution without clear evidence of bimodality. This is similar to that found in some other GCSs, such as NGC 1427 (Forte et al. 2001). We return to this point in Section 4.2. The GC candidates show a large spread in the $(g' - r')$ versus $(r' - i')$ plane. We have found eight marginally resolved objects with colours consistent with GCs. Curiously, all of these objects are very red and only found in field 1.

Regarding UCD candidates, there are eight candidates with luminosities $M_I > -15$. Two are type I and six are type II. The classification, however, is tentative because of the large spread of these objects in the colour–colour diagrams. We have also found one marginally resolved UCD candidate. Norris & Kannappan (in preparation) have confirmed one UCD object, which was not included in our sample because it is redder than our colour cuts.

4.1.4 NGC 3115

This galaxy shows the most obvious bimodality in our sample except for the brightest GCs ($M_I < -10.5$). Curiously, the CMD shows that the red GCs do not reach the same low luminosities as the blue GCs. In turn, the colour–colour diagram defines a very thin sequence with two GC clumps (as in the case of NGC 4649).

We also find a noticeable number of resolved GC candidates. A total of 38 objects fall in this category, and some of them clump at $M_I < -11$. It is interesting to note that most of these objects are confirmed as GCs by Kuntschner et al. (2002) and Puzia et al. (2004). There is one resolved UCD candidate (presented as a GC in Puzia et al. 2004) and seven unresolved UCDs. One of these is type I, and the remaining are type III.

4.1.5 NGC 3379

This is the poorest GCS and the least massive galaxy in our sample. However, bimodality is detectable even in the $(g' - r')$ versus $(r' - i')$ plane.

There are three marginally resolved GC candidates and three possible UCDs but all were classified as type III objects. One object, with $M_I \sim -12$ and $(g' - i')_0 \sim 0.8$ (which was spectroscopically confirmed by Pierce et al. 2006a as a GC), lies in the transition region between bright GCs and UCDs. We do not find any resolved UCDs. Some of the other bright GC candidates are indeed confirmed as such by Bergond et al. (2006) and Puzia et al. (2004). Therefore, this low-mass system also shows a detectable population of very massive GCs.

4.2 Colour histograms

Raw $(g' - i')_0$ colour distributions for all GC candidates selected as indicated in Section 4.1 are presented in the left panels of Fig. 5, ordered by decreasing B_T brightness of the host galaxy. These histograms were built by counting the objects in bins of 0.06 (NGC 4649, 3923, 524 and 3115) and 0.08 mag (NGC 3379), depending on the total number of candidates in each sample (dotted lines in Fig. 5). Additionally, a smoothed colour distribution was created by replacing each object by a Gaussian of $\sigma = 0.04$ mag (solid lines in Fig. 5). This σ value was considered to be representative of the mean error in $(g' - i')$ colours for fainter candidates. Each histogram is background-corrected, as described in the following, and the distributions of the contaminant objects are plotted as dashed lines.

For the case of NGC 4649, we adopted the WHDF as our control field. In all other cases, the average of counts in the WHDF and our CF was taken as representative of the background and subtracted.

As noted in Section 3.4, MW stars are the most important source of contamination for $i'_0 < 23.5$, while unresolved background galaxies are the main contaminants at fainter magnitudes. However, none of the targets listed in Table 1 is at very low galactic latitudes and the expected contamination level is probably less than 10 per cent (as demonstrated by our previous spectroscopic results).

The left panels of Fig. 5 show that, except for NGC 524, all the GCSs appear bimodal. NGC 4649 and 3115 show very well-defined blue and red peaks of $(g' - i')_0 \sim 0.75$ and $(g' - i')_0 \sim 1.0 - 1.1$. NGC 3923 appears bimodal, but the separation between peaks is less clear. NGC 3379 shows a marked blue peak around $(g' - i')_0 \sim$ 0.7–0.75, and a less conspicuous red population.

As noted before, NGC 524 is the only target where no clear bimodality is seen. However, its colour distribution looks rather broad and further high-quality photometry will be required to clarify the situation.

As shown in Fig. 1, the areal coverages are different in each observed GCS. As a consequence of this, we have attempted to recover the global colour distribution of the entire GCS by correcting for areal incompleteness. In order to do this, we split each GCS into different galactocentric radial bins. As seen in Section 3.3, the inner regions always have lower photometric completeness. We therefore exclude the zones within $R_{\rm gal} < 45$ arcsec. The outer zones have very small areal completeness (and hence introduce noise), so the points with $R_{\rm gal} > r_{\rm max}$ were also excluded. Here, $r_{\rm max}$ was taken as $R_{\rm gal}$, which shows areal completeness smaller than 20 per cent (in Table 4, we list the values of $r_{\rm max}$ for each GCS). After this, we calculated the fraction of each ring 'effectively' observed. Then, the inverse of these fractions was used as a correction factor. The number of radial bins was three in the two most massive galaxies (NGC 3923 and 4649), and two in the other less populated ones (NGC 3115, 3379 and 524). Finally, the total colour distribution was obtained by adding the colour distributions of each individual radial bin.

In the right panels of Fig. 5, we show the resulting background corrected histograms and smoothed colour distributions. The areal corrections lead to more prominent blue GCs populations. This results from the fact that blue GCs are less concentrated towards the centre of the host galaxy than the red GCs.

In the case of NGC 3923, the CMD shows a unimodal colour distribution for the brightest GCs. Then, we have split the sample

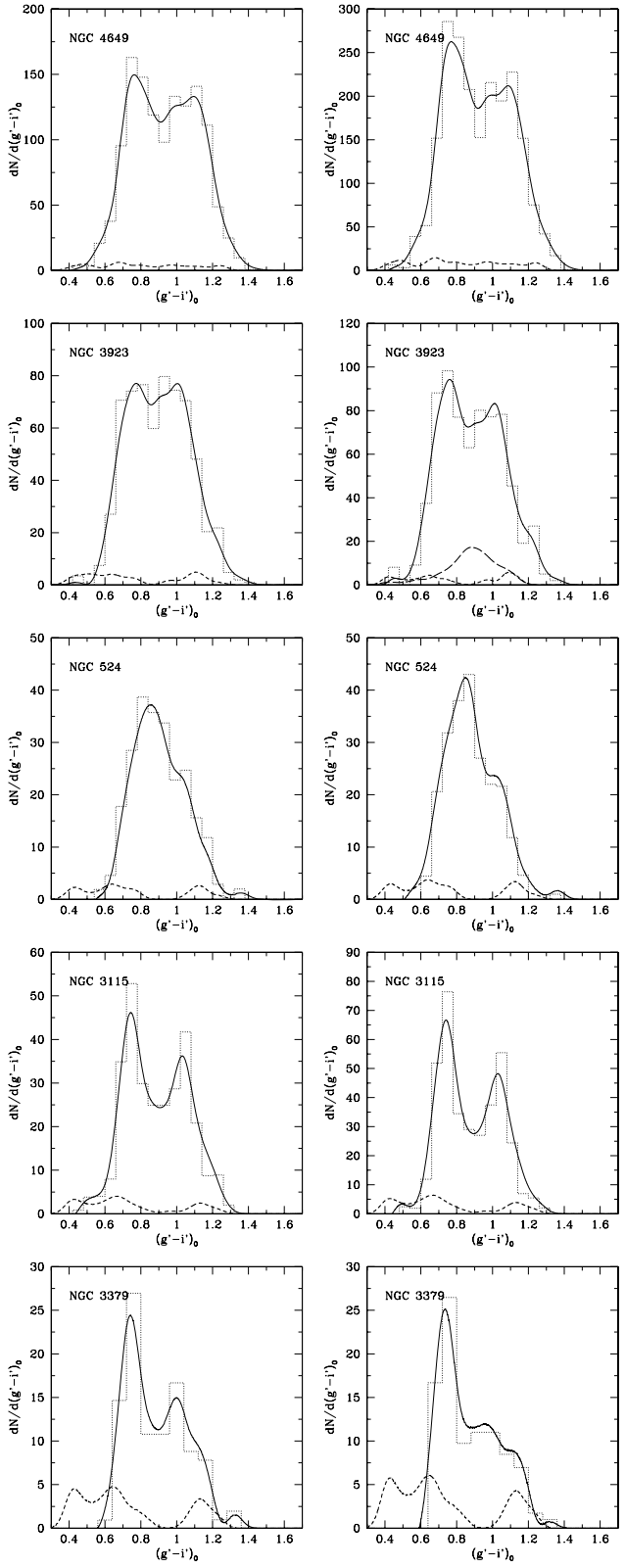

Figure 5. Left panels: dotted lines are the $(g' - i')_0$ colour histograms of all our GC candidates selected from samples with a 90 per cent completeness level. The solid lines are smoothed colour distributions, obtained as described in the text. The backgrounds used to correct the counts are shown as the dashed lines. Right panels: the same as the left panels, but corrected for areal completeness, as described in the text. In the case of NGC 3923, GCs brighter than $M_I = -11$ are shown as a long-dashed line.

into GCs having $M_I < -11$ (long-dashed line in Fig. 5) and $M_I > -11$ (the same codes as the other GCSs). Doing this, we see that the bright GC candidates are not bimodal. For NGC 3115 and 3379, the small number of bright GCs prevents a similar analysis.

In order to characterize the presence of bimodality in the integrated GC colours, we have run RMIX on our histograms (MacDonald 2007). This program allows the user to choose the type of distribution, the number of components and constraints. In this work, we adopted two normal components, allowing RMIX to fit the position of the peak, the standard deviation and the number of GC candidates in each populations. Using reasonable starting values, in all cases RMIX converged easily, so we did not constrain any parameter. The results are shown in Table 4. As a comparison, we list the modal values for all the GCSs showing two clear peaks in their colour distribution. In the case of NGC 4649, we list two values for each parameter. The first set of values is obtained using the whole sample, and the second taking GC candidates with $21.5 < i'_0 < 23.9$. In this last sample, both peaks are bluer. In particular, the blue peak moves 0.025 mag as a consequence of the 'blue tilt' phenomenon.

In the case of NGC 524, we specifically tested different types of fit. We found that a double Gaussian distribution fit was strongly preferred over only one leading to a χ value 2.7 times smaller. This supports the conclusion that NGC 524 is also a bimodal system. However, the blue peak in this galaxy $[(g' - i')_0 = 0.815 \pm 0.021]$ is the reddest in our sample. Deeper photometry could help us to obtain a more conclusive result for this galaxy.

Fig. 6 shows the positions of the GC colour peaks for the different cluster populations, as listed in Table 4, versus the galaxy M_B. Blue and red peaks are depicted as filled triangles and squares, respectively. One of the most striking characteristics of this figure is that the red peak of NGC 3923 seems to be too blue according to its absolute magnitude. To complement this, we have included the values corresponding to NGC 3311 as open and filled circles (Wehner et al. 2008). The following (error-weighted) linear fits were obtained for the red (equation 4) and blue (equation 4) GC peaks:

$$(g' - i')_0 = -0.03(\pm 0.01)M_B + 0.42(\pm 0.33); \quad (4)$$

$$(g' - i')_0 = -0.01(\pm 0.01)M_B + 0.56(\pm 0.22). \quad (5)$$

These fits are shown as solid lines in Fig. 6 where we also include the peaks corresponding to M87 from Harris (2009a) for comparison (open and filled stars). The M87 points are very consistent with our relations. However, it is important to note that Harris (2009a) calibrated his M87 photometry with Sloan Digital Sky Survey (SDSS) stars. As a result, some mismatch may be expected.

Peng et al. (2006) found that the slopes of $(g - z)$ versus M_B relations were -0.036 and -0.026 for red and blue peaks, respectively. Using some common objects between Jordán et al. (2009) and our NGC 4649 photometry, we have found that $d(g - z)/d(g' - i') = 1.36 \pm 0.05$. With this value, the slopes from Peng et al. translate to -0.026 and -0.019. Comparing with equations (4) and (5), we see that the red values are in very good agreement. However, our results for the blue peaks are consistent with no correlation.

We note that Peng et al. (2006) obtain $[\mathrm{Fe/H}] \propto L^{0.26\pm0.03}$ for the red GCs, which is identical to our value after adopting the colour–metallicity relation given in the next section.

4.3 Blue tilt

As noted in Section 4.1, NGC 4649 is the only galaxy in the sample where the blue GCs show a clear colour–magnitude trend, a feature called the 'blue tilt', and noticed by Strader et al. (2006) and Harris

Table 4. RMIX fits to the $(g' - i')_0$ colour distributions. The mean colours of the two modes μ_b (blue) and μ_r (red), their dispersions σ_b and σ_r and the fraction of objects assigned by RMIX to the blue GC population are listed. The last two columns give the galactocentric radii of the annuli, which show areal completeness smaller than 20 per cent, and the fraction of area effectively observed within those radii.

Galaxy	Modal values		rmix					r_{max}	f_T
	μ_b	μ_r	μ_b	σ_b	μ_r	σ_r	f_b	(arcsec)	
NGC 4649	0.765	1.095	0.783 ± 0.006	0.098 ± 0.004	1.080 ± 0.008	0.110 ± 0.004	0.518 ± 0.024	490	0.41
			0.758 ± 0.007	0.096 ± 0.004	1.067 ± 0.008	0.127 ± 0.004	0.442 ± 0.025	490	0.41
NGC 3923	0.758	1.011	0.746 ± 0.011	0.072 ± 0.008	1.005 ± 0.023	0.135 ± 0.014	0.365 ± 0.069	350	0.58
NGC 524	–	–	0.815 ± 0.021	0.086 ± 0.011	1.033 ± 0.040	0.076 ± 0.021	0.713 ± 0.120	315	0.70
NGC 3115	0.764	1.053	0.765 ± 0.007	0.067 ± 0.005	1.044 ± 0.011	0.092 ± 0.008	0.521 ± 0.037	320	0.58
NGC 3379	0.769	–	0.765 ± 0.009	0.036 ± 0.008	1.010 ± 0.029	0.135 ± 0.018	0.408 ± 0.082	290	0.72

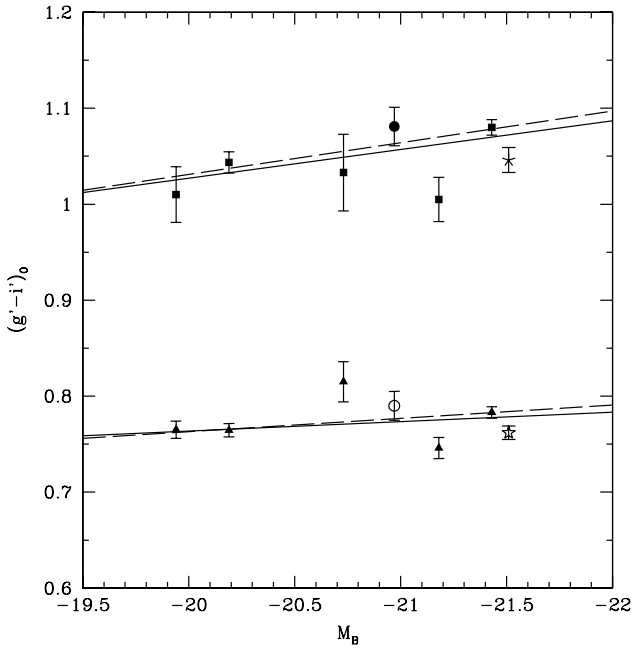

Figure 6. $(g' - i')_0$ colour for blue (filled triangles) and red peaks (filled squares) obtained by fitting two Gaussians to the colours histograms. We have included here the NGC 3311 (open and filled circles) and M87 (open and filled stars) points from Wehner et al. (2008) and Harris (2009a), respectively. Solid lines are the fits obtained as indicated in the text. Dashed lines are the results excluding NGC 3923 ($M_B = -21.18$) in the fits.

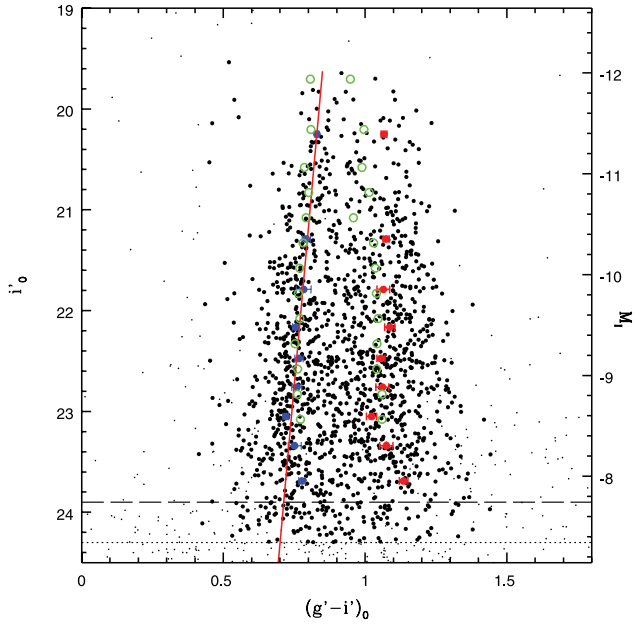

Figure 7. The 'blue tilt' in NGC 4649. Blue and red points are the positions of the peaks of the blue and red GC subpopulations obtained as indicated in the text. The green circles are those for the M87 GCS from Harris (2009a). The red line is a linear fit to the blue points for NGC 4649. Here we see that the blue tilt in this galaxy appears at $i'_0 \sim 23$ mag, which roughly corresponds to $M_I \sim -8.5$ mag.

et al. (2006). In contrast, all the other galaxies discussed in this paper show two broad colour sequences, without an obvious tilt (for a further study of the NGC 3923, see Norris & Kannappan 2011). The GC colour distributions in these galaxies become unimodal at bright magnitudes, a situation different from that in NGC 4649, where blue and red clusters are clearly separated even at higher luminosities.

In particular for NGC 4649, Strader et al. (2006) find a colour trend $d(g - z)/dz = -0.040 \pm 0.005$, identical, within the errors, to $d(g - z)/dz = -0.037 \pm 0.004$ derived by Mieske et al. (2006b), by combining the CMDs of M49, M60 and M87.

In order to characterize the 'blue tilt' in NGC 4649, using our GMOS photometry, we followed an approach similar to that described by Wehner et al. (2008). GCs were grouped in magnitude bins containing 150 clusters each and, using RMIX, we obtained the positions of the blue and red peaks. This procedure delivered nine pairs of values, depicted as blue and red dots in Fig. 7. In all the cases previously studied, the 'blue tilt' appears to have a similar behaviour. Fig. 7 shows that the blue sequence seems to become redder at a magnitude around $M_I \sim -9$ mag. In turn, and using a combined sample for six giant elliptical galaxies, Harris (2009b) found evidence that the 'blue tilt' starts to be detectable at absolute magnitudes brighter than $M_I = -9.5$ mag and exhibits a non-linear form. However, in our NGC 4649 sample, the three faintest points of the blue and red peaks (see Fig. 7) were not well constrained by RMIX as they have significant colour errors. So, these points were not included and only those with $i' < 23$ were used to perform linear fits to the blue and red GC groups:

$$(g' - i')_0 = -0.032(\pm 0.003) i'_0 + 1.478(\pm 0.072); \quad (6)$$

$$(g' - i')_0 = -0.007(\pm 0.006) i'_0 + 1.227(\pm 0.1356). \quad (7)$$

These fits indicate that the red GCs do not show a significant trend, as noted for other galaxies (Peng et al. 2009; Harris 2009a, b; Harris et al. 2010).

We stress that a second-order fit, like that performed by Harris (2009b), on our data produces very unstable solutions. However, we cannot rule out that the inclusion of a better sample of faint objects might require a higher-order fit.

As a comparison, Fig. 7 also includes the position of the blue and red peaks obtained by Harris (2009a) for the M87 GCS also using g and i photometry. Both galaxies exhibit remarkably similar blue tilts.

The fact that the tilt is detectable in some but not all galaxies is an issue that still deserves clarification. A tentative interpretation was presented by Forte et al. (2007), who showed that a large spread of the characteristic metallicity scale of the blue GCs smears the colour–magnitude relation in such a way that the tilt eventually becomes undetectable. In the specific case of the galaxies in our sample, the situation is not so clear. Although the CMDs for NGC 3379, 3115 and 524 in Fig. 4 show the presence of very massive GCs (those with $M_I < -10$ mag), their numbers are quite small, thereby preventing a meaningful detection of the blue tilt.

It is worth mentioning that Harris et al. (2010) found a well-defined tilt in the blue GC sequence in M104, using a sample with several hundred GCs. In contrast, NGC 3923, with a comparable number of clusters (∼670), exhibits no detectable tilt. This suggests that the size of the statistical sample cannot be the main reason for the absence of the tilt. We note, however, that our GC sample does not include a significant number of clusters brighter than $M_I \approx -9.5$, which conspires against the eventual detection of the tilt. Rather, our CMD suggests a 'unimodal' distribution for these bright clusters (however, see Norris & Kannappan 2011). Another question that deserves a more complete wide field analysis is why NGC 3923 seems to have a relatively sparse population of massive blue GCs.

We note that the 'blue tilt' has been identified as a possible instrumental artifact specifically affecting the *HST*/ACS photometry (Kundu 2008) and even dismissed on the basis of the $(V - I)$ photometry of M87 (Waters et al. 2009). However, the observations presented in this paper, together with other ground-based works (see also Forte et al. 2007, Wehner et al. 2008, Harris 2009a), and new *HST*/ACS-based analyses (Peng et al. 2009; Harris 2009b), strongly argue in favour of the existence of the blue tilt.

Previous works have presented an interpretation of the 'blue tilt' as the result of increasing metallicity with GC mass, i.e. a mass–metallicity relation (MMR). Bailin & Harris (2009) and Strader & Smith (2008) give models where the physical interpretation of the MMR is based on self-enrichment during a cluster's formation stage. According to these models, GCs with masses above 10^6 $M_\odot$ will hold on to enough of their supernova (SN) ejecta to enrich the gas from which stars are still being formed. A meaningful comparison of the results from different GCSs is somewhat precluded by the adoption of different colour–metallicity relations. The photometry presented in this paper, combined with our previous spectroscopic results (Pierce et al. 2006a, b; Norris et al. 2008), allows the determination of a new relation, which includes 67 globulars in three different galaxies (NGC 3923, 3379 and 4649). Chemical abundances [Z/H], obtained via Lick indices, are on the scale defined by the synthetic models by Thomas, Maraston & Korn (2004). Clusters fainter than $g'_0 = 23$ were rejected because of their relatively large associated errors.

The [Z/H] versus $(g' - i')_0$ values for the calibrating GCs are plotted in Fig. 8 where a linear fit

$$[Z/H] = 3.51(\pm 0.21)(g' - i')_0 - 3.91(\pm 0.20) \quad (8)$$

is also shown. The overall trend is in agreement with a rediscussion of the $(C - T_1)_0$ versus [Fe/H] relation presented in Forte et al. (2007) and with other works where more complex functions were fitted (e.g. Peng et al. 2006; Lee et al. 2008; Blakeslee, Cantiello & Peng 2010). However, it is worth emphasizing that all these last calibrations include higher-order colour terms, mostly set by low-

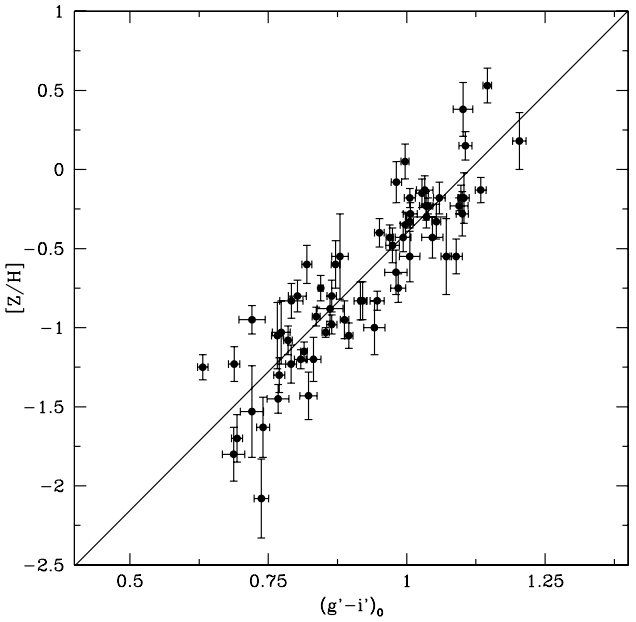

Figure 8. GC colour–metallicity relation. The points are GCs from the photometry presented in this work and metallicities from Pierce et al. (2006a, b) and Norris et al. (2008). The solid line is a linear fit (see the text).

metallicity MW globulars, whose counterparts are scarce in Fig. 8. A more direct comparison is possible using the recently published relation obtained by Sinnott et al. (2010). Those authors have used integrated colours in the USNO photometric system (Smith et al. 2002) and spectroscopically measured abundances of GCs from NGC 5128 and the MW. Their linear $(g' - i')_0$ versus [Fe/H] relation can be easily translated to the form of equation (8) using the [Fe/H] = [Z/H] − 0.131 relation from Mendel, Proctor & Forbes (2007), leading to $[Z/H] = 3.65 \times (g' - i')_0 - 4.18$, which compares very well with our results.

The adoption of a constant (M/L) ratio for the blue clusters, and the above calibration, leads to

$$Z \propto M^{0.28\pm0.03}, \quad (9)$$

in agreement with Mieske et al. (2006b) who, in the particular case of NGC 4649, derive an exponent of 0.36 ± 0.11.

Our colour–abundance relation was also applied to the g' and i' photometry presented by Cockcroft et al. (2009) for NGC 5193, IC 4329 and NGC 3311, leading to exponents of 0.23 ± 0.14, 0.37 ± 0.05 and 0.47 ± 0.03, respectively. These values are, on average, 30 per cent smaller than the exponents obtained by Cockcroft et al. These differences are typical of the uncertainties connected with the adoption of different metallicity scales.

4.4 Spatial distributions

Fig. 1 shows some already known systematics regarding the spatial distribution of both GC families (i.e. blue clusters usually exhibit relatively shallow distributions in contrast with those of red clusters, which are frequently more concentrated toward the galaxy centres).

In this section, we aim to quantify the spatial distributions through an analysis of the projected cluster density as a function of galactocentric distance using both a de Vaucouleurs law ($r^{1/4}$) and a power law. We also present Sérsic law fits in the case of the two brightest galaxies for which we have a good areal coverage.

Blue and red GCs were separated according to a common 'colour valley' at $(g' - i')_0 \sim 0.95$ and the limiting i'_0 magnitude was set at the 90 per cent completeness level. Because of their relatively low flattenings, we used circular annuli with $\Delta \log r = 0.1$–0.15 for all galaxies except NGC 3115, for which we adopted an ellipticity of 0.55.

The resulting areal density distributions are displayed in Fig. 9, and the fit parameters are listed in Table 5. As a general comment, we point out that both the de Vaucouleurs and the power law give very similar results in terms of the residual errors, although the former yields marginally better fits in the innermost regions.

In the cases of NGC 4649 and 3923, our observations were combined with the *HST*/ACS data, allowing a fit to the innermost regions. The GC candidates from Jordán et al. (2009) were used for NGC 4649, and in NGC 3923 the clusters were selected from our own analysis of the same ACS archive images used by Sikkema et al. (2006). The ACS and GMOS profiles were matched by normalizing the counts in common selected radial annuli.

For these galaxies, Sérsic law fits in the form $\log \sigma(r) = s_1 + s_2 * r^N$ are also shown in Fig. 9. The respective s_1, s_2 and N values are -0.57 ± 0.19, -0.27 ± 0.09 and 0.36 ± 0.04 for NGC 4649, and -0.60 ± 0.20, -0.51 ± 0.20 and 0.26 ± 0.09 for NGC 3923.

A core-like distribution is detected in the case of NGC 4649, similar to that found, for example, in M87 by Lauer & Kormendy (1986) and Kundu et al. (1999). In turn, the Sérsic law seems compatible with a de Vaucouleurs fit along the whole galactocentric range in NGC 3923.

Here, we give some brief comments about the characteristics of each galaxy.

4.4.1 NGC 4649

Our density profile improves that already presented in Forbes et al. (2004) because of a better determination of the level of the subtracted background. The slope values given in Table 5, in turn, are in excellent agreement with those presented by Lee et al. (2008).

4.4.2 NGC 3923

Both Figs 1 and 9 show that the blue globulars have a very shallow distribution. In fact, the slope of the density profile for these clusters is the lowest in our sample. Sikkema et al. (2006) also found very low values, although their photometry only includes the central region of the galaxy.

This feature deserves some attention as it may be connected with the merger history of this galaxy as suggested by the well-known ripples detectable in its brightness profile (see Malin & Carter 1980).

4.4.3 NGC 524

As mentioned previously, the colour histogram of the GCs in this galaxy do not show a clearly detectable bimodality. For this reason, the density profile displayed in Fig. 9 corresponds to the whole cluster population. The derived value is consistent with that of Harris & Hanes (1985).

We note, however, that an inspection of the innermost region in this galaxy indicates that the red GCs seem very concentrated (a situation that resembles the case of NGC 1427; Forte et al. 2001). However, when splitting the sample at $(g' - i')_0 = 0.9$, as shown by Fig. 1, the 'reddest' GCs exhibit a clump inside $R_{\rm gal} < 1$ arcmin. In contrast, this feature is absent in the 'blue' clusters.

4.4.4 NGC 3115

This galaxy exhibits a high flattening and its GCs seem to follow the brightness isophotal contours. However, our uneven spatial coverage does not allow a quantitative confirmation (e.g. via azimuthal counts).

4.4.5 NGC 3379

Because this galaxy shows a very low number of GC candidates, the density profile displayed in Fig. 9 corresponds to the whole GC population. The resulting slope is steeper than that given by Rhode & Zepf (2004), who found -1.4 in their wide field study. This could indicate a difference in the background levels adopted in these two studies.

Fig. 1 shows that the blue and red candidates in this galaxy are not homogeneously distributed around the centre. The red GCs show a clump to the north-east, while the blue GCs are clearly less numerous in that region. This inhomogeneous distribution is also seen in Whitlock et al. (2003) (their fig. 3).

4.5 Galactocentric colour trends

Fig. 10 shows the $(g' - i')_0$ colours of all the GC candidates brighter than the 90 per cent completeness level as a function of the normalized galactocentric radius $R_{\rm gal}/R_{\rm eff}$, where $R_{\rm eff}$ is the effective radius in the B band taken from RC3 data in the NASA/IPAC Extragalactic Data base (NED).

The mean colours for each GC family were obtained within galactocentric bins of variable size (containing the same number of clusters) and fit with a logarithmic law:

$$(g' - i')_0 = a \log(R/R_{\rm eff}) + b. \quad (10)$$

The a and b parameters are listed in Table 6, along with the associated uncertainties obtained through a least-squares fit, for each GC subpopulation except for NGC 3379 where, because of the low number of clusters, blue and red GCs were grouped together. The listed colour gradients were combined with equation (8) to obtain values of $\Delta[{\rm Z/H}]/\log(R/R_{\rm eff})$ and are included in Table 6.

The overall appearance of Fig. 10 suggests very mild gradients over a galactocentric range larger than $\approx$1–2 $R_{\rm eff}$. A similar trend has been noted by Harris (2009a, b) in M87 and six other GCSs belonging to giant elliptical galaxies. Beyond this, each galaxy has its own and distinct behaviour. In particular, NGC 524 and 3115 (both S0 galaxies) exhibit the highest colour gradients in their innermost regions (Tortora et al. 2010).

Fig. 10 also includes the $(g' - i')_0$ halo colours derived from our images. They were obtained within the central 2 arcmin of the galaxies because this zone is not strongly affected by the sky level adopted. These colours are remarkably similar to the mean colours of the red GCs, a similarity already noted in the inner regions of several galaxies (see, for example, Forbes & Forte 2001).

Our data add to the increasing evidence in the literature for colour, and hence metallicity, gradients in the individual GC subpopulations (e.g. Harris 2009b; Forbes et al. 2011; Liu et al. 2011). Such gradients are indicative of a dissipative formation process for both GC subpopulations. In a detailed study of the NGC 1407 GCS, Forbes et al. (2011) suggested that a transition occurred between the inner region with strong GC

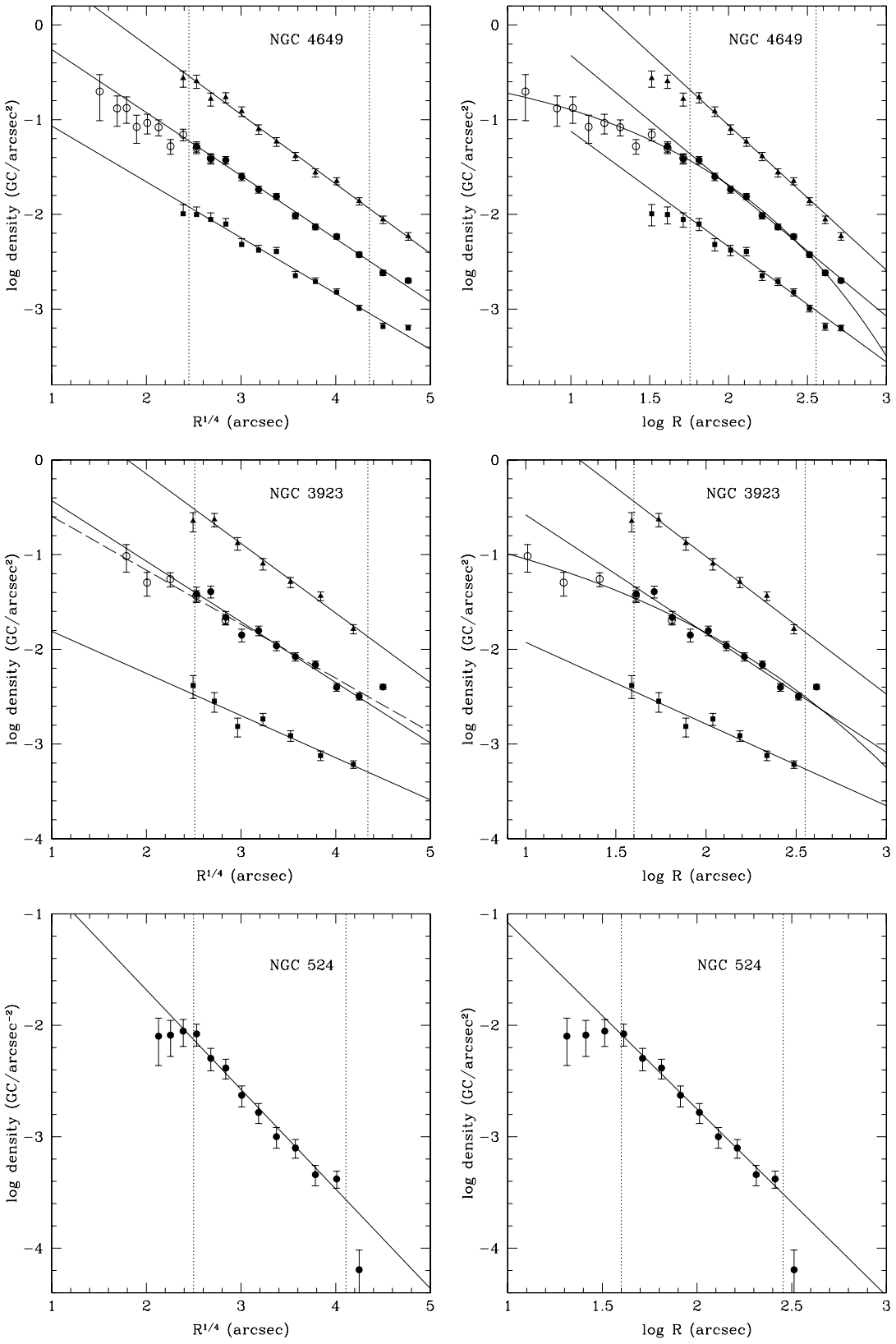

Figure 9. Projected radial profiles for all (filled circles), red (triangles) and blue GC candidates (squares) fit with a de Vaucouleurs law (left panels) and with a power law (right panels). The profiles were arbitrarily shifted in order to avoid overlapping. Because NGC 3379 shows a very low number of red GCs and NGC 524 does not show a clear 'valley', their GC samples were not split into red and blue subpopulations. In the case of NGC 3115, the projected density profile was obtained in elliptical rings. Dashed lines indicate the radial ranges included in the fits. Open circles in the NGC 4649 and 3923 figures are from ACS photometry (see text).

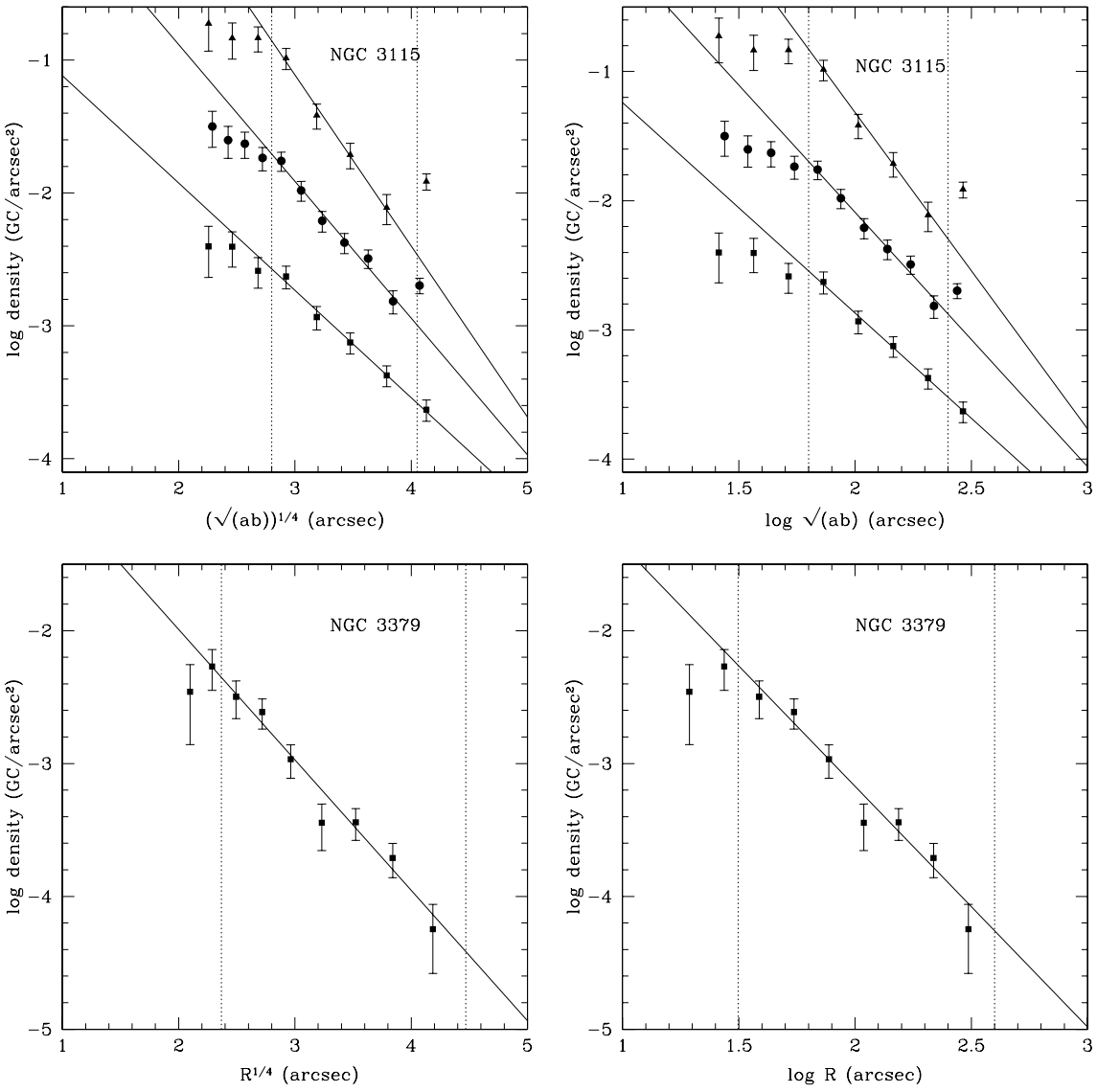

Figure 9 – *continued*

Table 5. Slopes and errors of the surface density profiles of all, red and blue GC candidates obtained using a weighted least-squares method. We list the results for a power law and the de Vaucouleurs law.

Galaxy	All		Red		Blue	
	Power law	de Vaucouleurs	Power law	de Vaucouleurs	Power law	de Vaucouleurs
NGC 4649	-1.37 ± 0.04	-0.67 ± 0.02	-1.52 ± 0.04	-0.73 ± 0.02	-1.21 ± 0.08	-0.58 ± 0.03
NGC 3923	-1.25 ± 0.07	-0.64 ± 0.03	-1.45 ± 0.09	-0.73 ± 0.04	-0.86 ± 0.08	-0.44 ± 0.05
NGC 524	-1.67 ± 0.06	-0.89 ± 0.05	–	–	–	–
NGC 3115	-1.59 ± 0.13	-0.78 ± 0.07	-1.74 ± 0.17	-1.08 ± 0.10	-1.45 ± 0.15	$- 0.73 \pm 0.07$
NGC 3115 (ellip)	-1.97 ± 0.12	-1.02 ± 0.05	-2.45 ± 0.11	-1.28 ± 0.08	-1.62 ± 0.05	-0.81 ± 0.04
NGC 3379	-1.81 ± 0.16	-0.98 ± 0.08	–	–	–	–

gradients and an outer region with no colour gradient. This was interpreted as support for the two phase formation model of early-type galaxies (Oser et al. 2010) in which such galaxies are built up from a dissipative core that experiences later accretion. Our data show shallower gradients and fewer GCs than detected in NGC 1407 by Forbes et al. Further data on a rich GCS, such as NGC 4649, would be needed to search for such a transition.

The GC colour gradients are also compared to the colour gradient of the underlying starlight in the galaxy. In each case, where the GCS can be clearly separated into two subpopulations, we find that the galaxy gradient matches the red GC subpopulation gradient in both absolute colour and in slope over a common radial range. This provides strong support for the idea that the red GCs are associated with the bulge/spheroid stars of early-type galaxies, and hence might

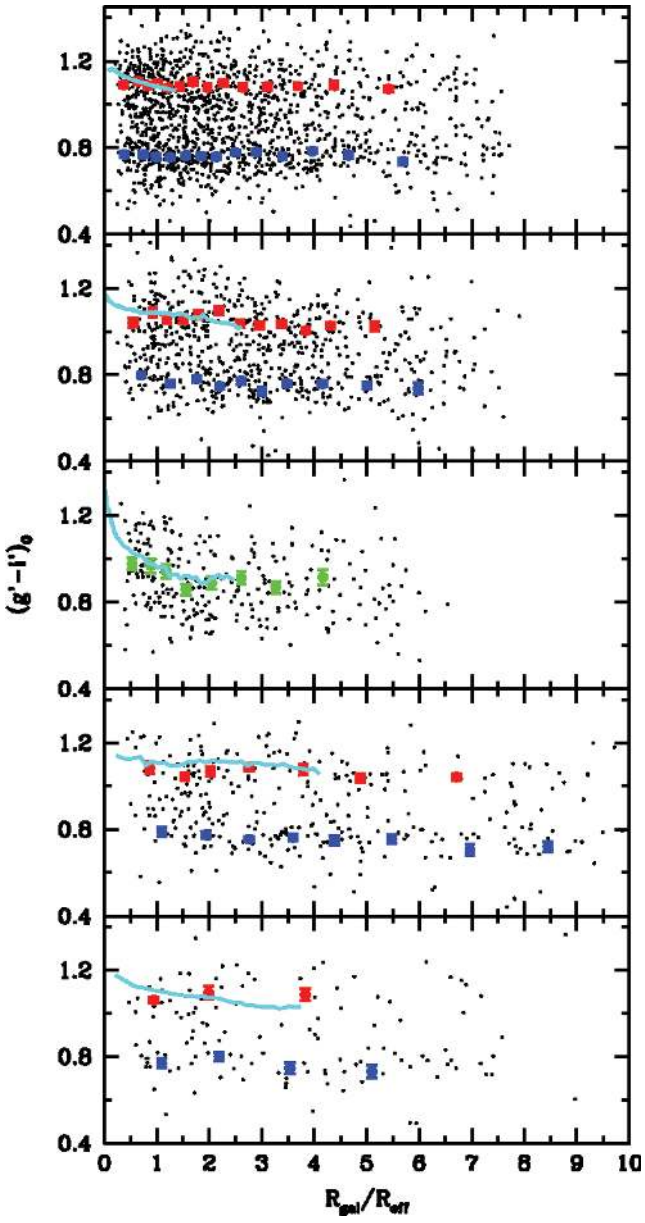

Figure 10. $(g' - i')_0$ colour index versus projected galactocentric distance normalized by $R_{\rm eff}$ (in the B band). The colour profile for each galaxy halo, within a radius of 2 arcmin, is shown as the solid line in each panel. From top to bottom: NGC 4649, 3923, 524, 3115 and 3379.

have shared a common formation epoch (Forbes & Forte 2001; Forte et al. 2009; Spitler 2010).

4.6 GC integrated luminosity functions and GC specific frequencies S_N

4.6.1 Integrated luminosity functions

In this section, we aim to determine the integrated GC luminosity function (GCLF) for each galaxy. Fig. 11 shows the raw and completeness corrected counts of cluster candidates as well as those of the adopted CF as a function of i'_0 magnitude. NGC 4649 and 3115 exhibit a good contrast at the expected turn-over magnitude (TOM) between clusters and contaminant objects, allowing this type of analysis. In NGC 3923, we do not have such a good contrast. However, the completeness and the background counts are good enough to try to recover some useful information. In NGC 3379, the low number of candidates and the strong dependence of the background adopted make it difficult to obtain reliable results, and the parameters of the GCLF are not very well constrained. For this reason, the points with $i' > 23.2$ were rejected from the fit. In the case of NGC 524, we expect to have the TOM at $i'_0 \sim 23.9$, where our photometry has a very low photometric completeness. Therefore, this galaxy was not included in what follows.

The resulting GCLFs, determined on the basis of the net counts within 0.25-mag bins, are displayed in Fig. 12, together with the normalized counts of the subtracted background.

Both a Gaussian and a t5 function fit were performed on each histogram in order to determine the position of the TOM and the dispersion parameter. As the results do not show clear differences between both approaches, we only give the parameters of the Gaussian fit in Table 7.

Reliable estimates of the TOMs in NGC 4649 and 3115 are derived as our adopted limiting magnitude is fainter than the TOMs by approximately 1 mag.

For these galaxies, we also obtained the TOMs of the blue and red GC populations defined in terms of the $(g' - i')_0$ 'valley' in the colour statistics. The corresponding corrected luminosity functions for each GC subpopulation are shown in Fig. 13. A comparison shows that, in NGC 4649, the blue and red TOMs are coincident within the errors. This agreement is expected as the i'_0 magnitudes are not strongly affected by metallicity effects (see Ashman, Conti & Zepf 1995). The situation is not clear in NGC 3115 where the blue TOM seems fainter than the red TOM, contrary to the expectations for two coeval GC populations with different metallicities. An inspection of Fig. 1 shows that our areal coverage of the central region of this galaxy is rather poor, resulting in the loss of a fraction of the red GC population (because red GCs are more concentrated towards the centre of the galaxy than blue GCs) and possibly producing a spurious effect on the magnitude statistics of these clusters.

For NGC 3923, and as the TOM seems very close to the magnitude cut-off (at a 50 per cent completeness level), we only derive the dispersion. In this case, we adopted the I-band TOM given by Kundu & Whitmore (2001), which, at the adopted distance modulus, becomes $i'_0 = 23.8 \pm 0.28$.

The adoption of the absolute TOM magnitudes given by Kundu & Whitmore (2001) and the use of the relation given in equation (1) lead to distance moduli $(m - M)_I = 30.92 \pm 0.06$ and $(m - M)_I = 29.75 \pm 0.09$ for NGC 4649 and 3115, respectively.

A comparison with Larsen et al. (2001), Kundu & Whitmore (1998) and Kundu & Whitmore (2001) (previous correction by the TOM for the MW GCs and the M_V adopted by these authors) shows excellent agreement between their distance moduli and ours.

4.6.2 Specific frequency and total GC population

Adopting Gaussian integrated luminosity functions defined by the parameters given in Table 7 in combination with the projected areal density profiles previously discussed, we derive the cumulative specific globular frequency $S_N = N_{\rm tot} 10^{0.4(M_V+15)}$ for each galaxy within maximum galactocentric radii of 50 and 100 kpc. The first radius seems a reasonable value in order to include most (if not all) the CGs associated with a given low-mass galaxy. The largest radius seems more appropriate for massive galaxies that have very extended GCSs (see, for example, Bassino et al. 2006; Harris 2009a).

Table 6. Slopes and errors of the mean $(g' - i')_0$ colours as a function of R_{gal}. These values were obtained by fitting the relation: $(g' - i')_0 = a \times \log(R_{gal}/R_{eff}) + b$. The [Z/H] gradients, obtained using equation (8), are listed in columns (4) and (5). In the cases of NGC 4649, 3923 and 3115, two values are listed. The first value shows the slopes obtained by using the entire sample of points showed in the figure, and the second corresponds to a fit excluding the inner point.

Galaxy	Slopes $(g' - i')_0$		Slopes [Z/H]		N_{bin}
	Red	Blue	Red	Blue	
NGC 4649	-0.015 ± 0.007	-0.001 ± 0.011	-0.052 ± 0.024	-0.004 ± 0.038	50
	-0.021 ± 0.009	0.004 ± 0.015	-0.073 ± 0.032	0.014 ± 0.052	50
NGC 3923	-0.050 ± 0.024	-0.051 ± 0.019	-0.175 ± 0.084	-0.179 ± 0.067	30
	-0.095 ± 0.024	-0.033 ± 0.025	-0.333 ± 0.086	-0.115 ± 0.088	30
NGC 524	$-0.099 \pm 0.043/-0.194 \pm 0.069$		$-0.347 \pm 0.152/-0.681 \pm 0.245$		30
NGC 3115	-0.030 ± 0.028	-0.076 ± 0.016	-0.105 ± 0.098	-0.266 ± 0.058	20
	-0.022 ± 0.037	-0.081 ± 0.024	-0.077 ± 0.130	-0.284 ± 0.085	20
NGC 3379	–	-0.066 ± 0.055	–	-0.232 ± 0.193	15

In order to estimate N_{tot} for NGC 4649 and 3923, we have integrated the de Vaucouleurs law profiles obtained by fitting the GMOS+ACS profile presented in Fig. 9. In the particular case of NGC 3115, we have integrated our de Vaucouleurs GMOS profile and we adopted the WFPC2 photometry given by Larsen et al. (2001) to complete the counts in the innermost regions of the galaxy not covered by our frames. As those density profiles were obtained by considering samples with 90 per cent completeness magnitude cuts, these three values were corrected by calculating the fraction of the GCLF not included beyond these magnitude limits.

Absolute galaxy luminosities were obtained using the photometric values given in the NED and the distance moduli listed in Table 1. The total number of GCs, galaxy visual luminosity and inferred S_N values are included in Table 7. As an indication of the uncertainty in our estimation of N_{tot} and S_N, we list as the error the difference between the results obtained by integrating a de Vaucouleurs and power-law profiles.

For NGC 4649, there are two previously published values of S_N in the literature, both of which were calculated for 50 kpc: $S_N = 3.8 \pm 0.4$ and $S_N = 4.1 \pm 1$ from Lee et al. (2008) and Forbes et al. (2004), respectively. A comparison with the numbers listed in Table 7 shows that our new S_N value agrees very well with these values.

For NGC 3923, Sikkema et al. (2006) have obtained $S_N = 5.6 \pm 1.3$ and $S_N = 8.3 \pm 3.6$, for the same two radial limits listed in Table 7. However, they have used a different distance and M_V for this target. Taking this into account, we have corrected their values and obtained $S_N = 3.4$ and $S_N = 5.05$, lower than those listed in Table 7.

For NGC 3115, the only previous estimation of the cumulative specific frequency is that from Harris & Harris (2011), $S_N = 2.0$, which is very similar to our results for this galaxy.

Rhode & Zepf (2004) and Harris & Harris (2011) have determined a value of $S_N = 1.2 \pm 0.3$ for NGC 3379, in good agreement with our result.

5 CONCLUSIONS

Deep GMOS multicolour photometry has been obtained for the GCSs of five early-type galaxies. The primary results of this study, which will be combined with the spectroscopic results for further discussion in a following paper, are as follows.

(i) All the studied GCSs show bimodal integrated colour distributions. Even the less clear case, NGC 524, appears bimodal when analysed with the RMIX software. The adoption of a mass-to-luminosity ratio $(M/L)_B = 8$ indicates a minimum stellar mass close to 1.2×10^{11} $M_\odot$ for our galaxy sample (i.e. all these systems are above the minimum mass where bimodality becomes detectable as a common feature; Peng et al. 2006).

(ii) The mean colours of the peaks of red GCs follow a well-defined luminosity–colour relation in the sense that these peaks become redder with increasing galaxy luminosity. This is indicative of a larger GC chemical abundance scale for the most luminous galaxies, which, being more massive, are also capable of a more efficient enrichment. We note that the most massive system in this work (NGC 4649) lies outside the plane defined by GCSs in the logarithmic three-dimensional space determined by galaxy stellar mass, projected stellar mass density and GC formation efficiency, possibly indicating a merger past history as suggested by Forte et al. (2009). The GC blue peaks, in turn, show no significant correlation or, possibly, only a very mild one, with galaxy luminosity a situation already noted in the literature (Peng et al. 2006).

(iii) An empirical $(g' - i')$ versus [Z/H] relation was obtained based solely on GMOS data. A linear fit yields [Z/H] = 3.51($\pm$ 0.21) $(g' - i')_0 - 3.91$ ($\pm$0.20), which provides a good approximation, although the eventual presence of a second-order term at the low-metallicity end will require the inclusion of more GCs.

(iv) A comparison of the colour spreads of both blue and red GCs, when transformed to metallicity, clearly indicates that both populations are widely different in terms of chemical abundance. When associated with the different spatial distributions of these subpopulations, this fact strongly indicates a distinct nature for the two populations.

(v) A number of resolved/marginally resolved GC candidates were detected in all five galaxies. Some are spectroscopically confirmed as GCs in the literature. In principle, the GC upper mass shows a dependence with galaxy luminosity (e.g. Villegas et al. 2010). Then, the detection of resolved clusters could be a more frequent situation in these systems. However, further analysis will require the inclusion of distance effects.

(vi) A population of UCD candidates (resolved and unresolved with $-15 < M_I < -12$) were also detected in all the galaxies. NGC 3923 shows the highest number of associated objects, followed by NGC 4649 and 3115. This result indicates that UCDs are indeed a common feature, although the small size of our sample does not allow a definite conclusion in statistical terms.

(vii) In this paper, we report on the first detection of the so-called 'blue tilt' in NGC 4649 using ground-based observations. As a first approach, we adopted a linear relation between GC

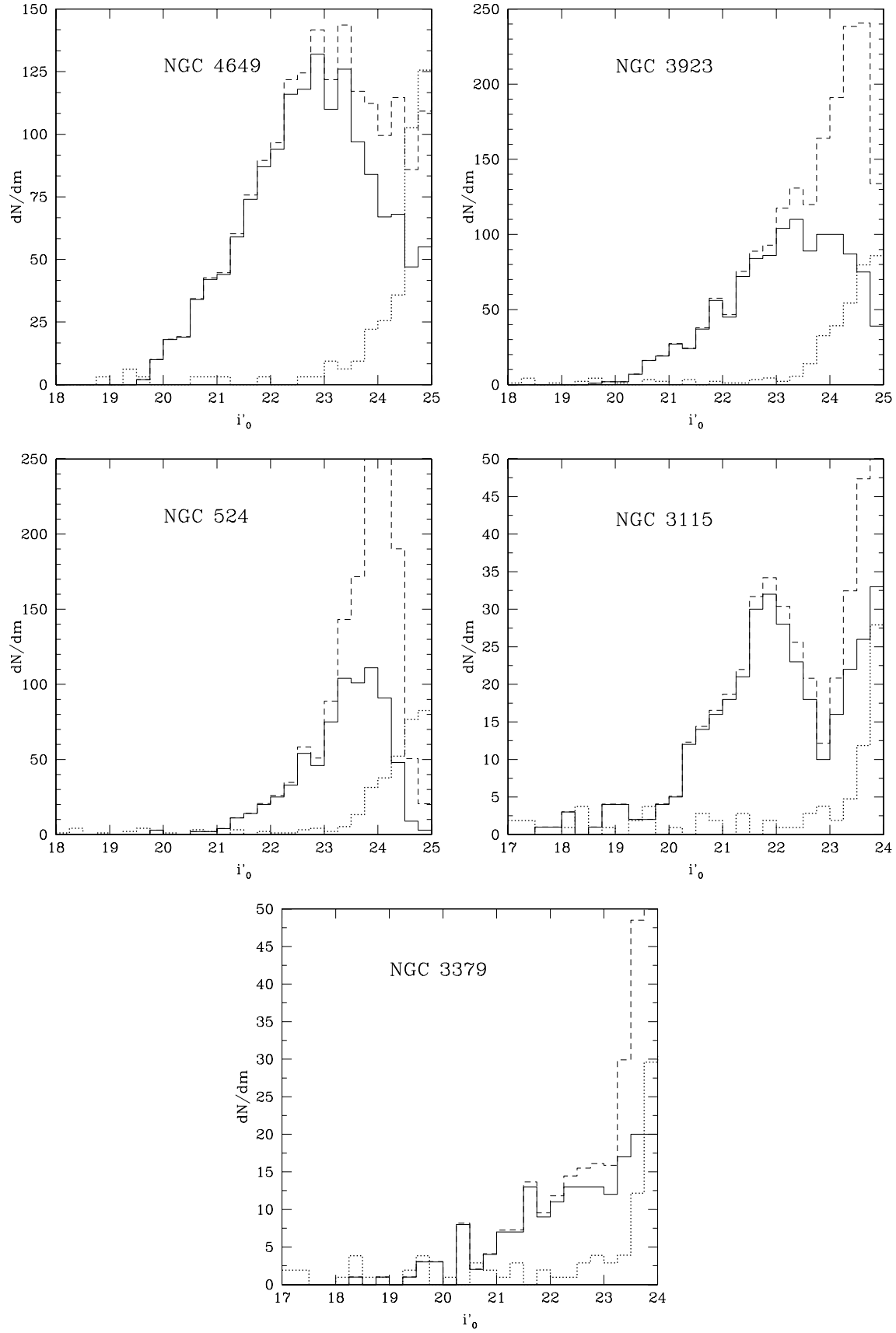

Figure 11. Raw counts (solid histograms) and completeness corrected counts (dashed line) for the five galaxies in the sample as a function of i'_0 magnitudes. The normalized backgrounds adopted in each case are shown as dotted lines.

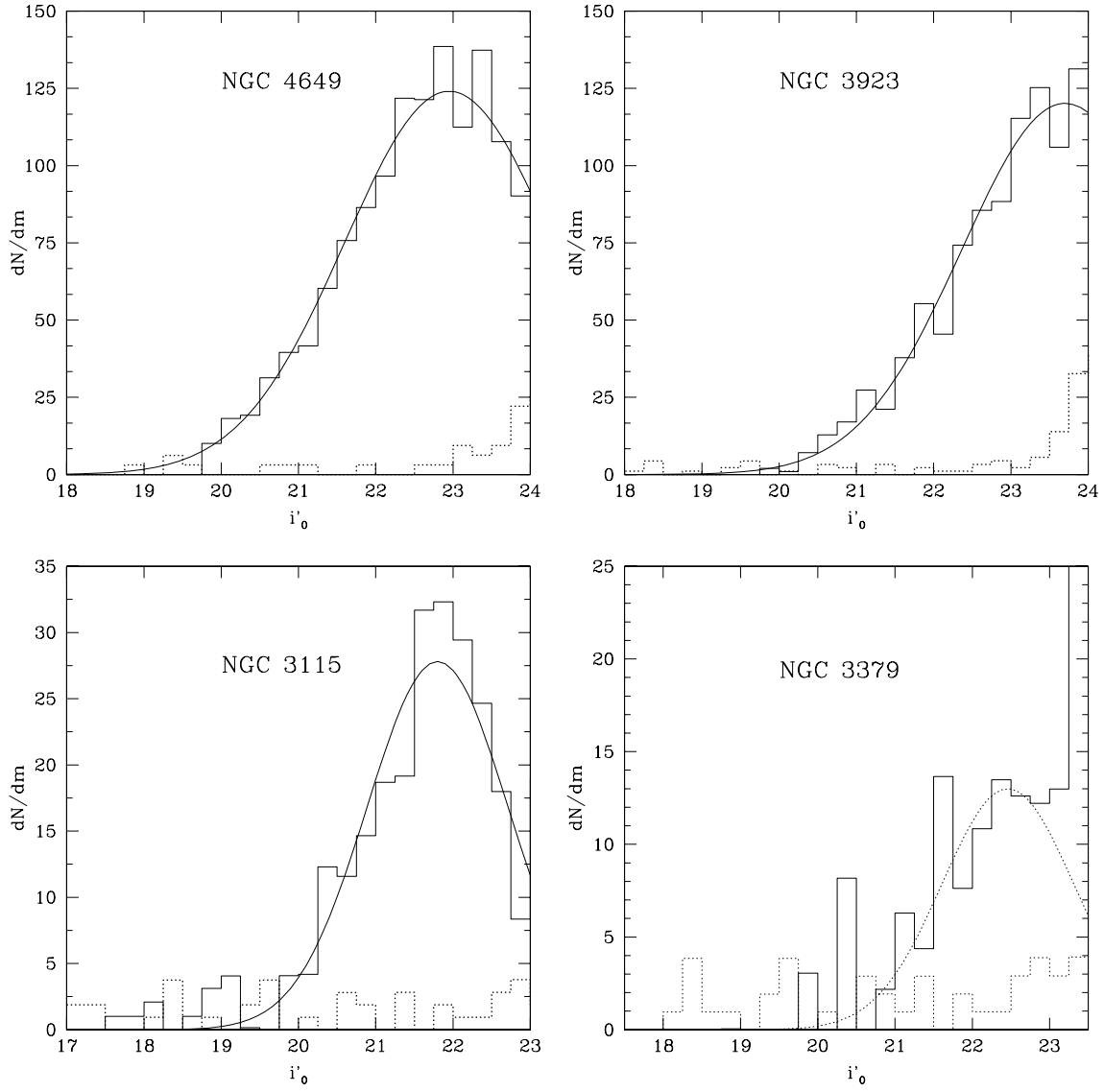

Figure 12. GCLFs in the i'_0 band. We show with solid lines the background and completeness corrected histograms of the GC candidates. The fitted Gaussian GCLFs are also shown as solid lines. The corresponding backgrounds are displayed as dotted histograms.

Table 7. Parameter for fitted Gaussian GCLFs. The last four columns give the total number of GCs and the specific frequency obtained considering limits of 50 and 100 kpc for the GCS.

Galaxy	TOM	σ	$\mathrm{TOM_{red}}$	σ_{red}	$\mathrm{TOM_{blue}}$	σ_{blue}	M_V	Nt_{50}	S_{N50}	Nt_{100}	S_{N100}
NGC 4649	22.95 ± 0.05	1.35 ± 0.05	22.92 ± 0.07	1.28 ± 0.09	22.96 ± 0.07	1.28 ± 0.09	-22.44	3310 ± 130	3.5 ± 0.1	4690 ± 980	5.0 ± 1
NGC 3923	23.84 (fixed)	1.42 ± 0.05	–	–	–	–	-22.03	3019 ± 70	4.1 ± 0.1	4580 ± 820	6.3 ± 1.1
NGC 3115	21.78 ± 0.08	0.91 ± 0.07	21.59 ± 0.07	0.71 ± 0.05	22.93 ± 0.15	1.04 ± 0.12	-21.13	546 ± 80	1.9 ± 0.2	571 ± 190	2.0 ± 0.7
NGC 3379	22.46 ± 0.37	0.85 ± 0.23	–	–	–	–	-20.88	216 ± 42	0.9 ± 0.2	226 ± 100	1.0 ± 0.4

colours and magnitudes, although, as shown by Harris (2009b) on the basis of a more numerous GCs sample, the tilt may exhibit some degree of curvature that becomes more evident for the brightest clusters. The tilt translates into an approximate mass–metallicity relation, given by $Z \propto M^{0.28\pm0.03}$. This result is in excellent agreement with the mean trend obtained by Cockcroft et al. (2009).

(viii) All the GCS density profiles are reasonably well fitted by a power law, although, in the case of NGC 4649, an $R^{1/4}$ dependence produces a better fit in terms of the residuals. As found in other galaxies, the red GCs show a more concentrated spatial distribution than the blue GCs, again lending support to the idea that bimodality is a real and distinctive feature and not a mere result of a particular colour–metallicity relation.

(ix) We confirm the very low spatial concentration of the NGC 3923 GCS found by Sikkema et al. (2006). In contrast to these authors, we find a significant difference of the areal density slopes of the red and blue GCs.

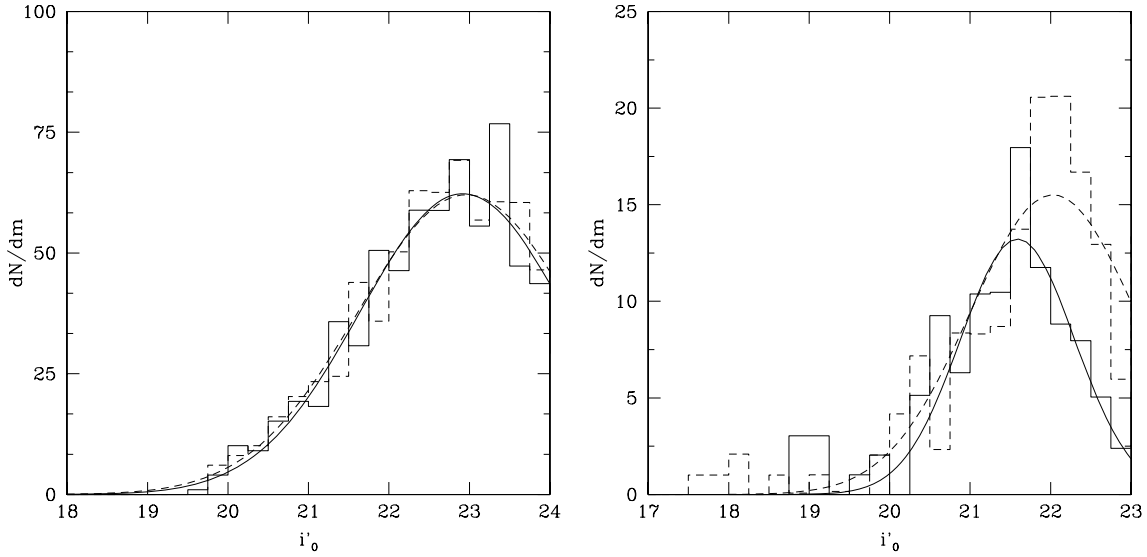

Figure 13. Corrected luminosity functions for each GC subpopulation in galaxies NGC 4649 (left) and NGC 3115 (right). The luminosity functions for red GCs are shown as solid lines and those for blue GCs as dashed lines.

(x) We have measured radial colour gradients for the blue and red GC subpopulations separately, and we find evidence for statistically significant gradients in several galaxies out to several effective radii (tens of kpc). The steeper gradients are those present in the two S0 galaxies included in the sample. These galaxies have smaller stellar masses than the brightest ellipticals in this study showing shallower gradients. This is in agreement with Tortora et al. (2010), who find a non-monotonic behaviour of colour gradients with galaxy mass. A possible interpretation of this trend assumes that more massive galaxies may have experienced mergers that lead to a dilution of the chemical gradients.

(xi) As in other studied systems, the red GC subpopulation has similar colours to the galaxy halo stars in their inner region. This is consistent with the idea that most of the galaxy luminosity in these regions comes from a diffuse stellar population associated with these clusters (e.g. Forte et al. 2007).

(xii) The TOM and σ were determined for the GCLF of NGC 4649 and 3115. In the case of NGC 3923, only σ was fitted. This parameter and the density profiles were used to obtain the total GC populations, and the specific frequency S_N of these galaxies. The highest $S_N = 4.5$ value was obtained for NGC 3923, followed by NGC 4649, $S_N = 3.6$. We have obtained new estimations of the NGC 3115 and 3379 specific frequencies, $S_N = 2.0 \pm 07$ and $S_N = 1.0 \pm 0.4$, respectively.

ACKNOWLEDGMENTS

FF acknowledges financial support from the Agencia de Promoción Científica y Tecnológica (BID AR PICT 885). This work was partially supported by CONICET funds through a PIP 2009/712 grant. SEZ acknowledges support for this work in part from the NSF grant AST-0406891. Data were based on observations obtained at the Gemini Observatory, which is operated by the Association of Universities for Research in Astronomy, Inc., under a cooperative agreement with the NSF on behalf of the Gemini partnership: the NSF (United States), the Particle Physics and Astronomy Research Council (United Kingdom), the National Research Council (Canada), CONICYT (Chile), the Australian Research Council (Australia), CNPq (Brazil) and Ministerio de Ciencia, Tecnología e Innovación Tecnológica (Argentina). The Gemini programme IDs are GN-2007A-Q-37, GS-2007A-Q-49, GN-2002B-Q-25, GN-2003A-Q-22, GS-2004A-Q-9 and GN-2001B-SV-104. This research has made use of the NED, which is operated by the Jet Propulsion Laboratory, Caltech, under contract with the National Aeronautics and Space Administration.

REFERENCES

Ajhar E. A., Tonry J. L., 1994, ApJ, 429, 557
Ashman K. M., Zepf S. E., 1992, ApJ, 384, 50
Ashman K. M., Conti A., Zepf S. E., 1995, AJ, 110, 1164
Bailin J., Harris W., 2009, ApJ, 695, 1082
Bassino L., Faifer F., Forte J., Dirsch B., Richtler T., Geisler D., Schubert Y., 2006, A&A, 451, 789
Beasley M. A., Baugh C. M., Forbes D. A., Sharples R. M., Frenk C. S., 2002, MNRAS, 333, 383
Beasley M., Forbes D., Brodie J., Kissler-Patig M., 2004, MNRAS, 347, 1150
Bergond G., Zepf S. E., Romanowsky A., Sharples R., Rhode K., 2006, A&A, 448, 155
Bertin E., Arnouts S., 1996, A&AS, 117, 393
Blakeslee J. P., Cantiello M., Peng E. W., 2010, ApJ, 710
Bridges T. et al., 2006, MNRAS, 373, 157
Brodie J. P., Strader J., 2006, AR&A, 44, 193
Buote D. A., Canizares C. R., 1999, MNRAS, 298, 811
Cockcroft R., Harris W., Wehner E., Whitmore B., Rothberg B., 2009, AJ, 138, 758
Couture J., Harris W. E., Allwright J. W. B., 1991, ApJ, 372, 97
Denicoló G., Terlevich R., Terlevich E., Forbes D. A., Terlevich A., 2005, MNRAS, 358, 813
de Vaucouleurs G., de Vaucouleurs A., Corwin H. G., Buta R. J., Paturel G., Fouque P., 1991, Third Reference Catalogue of Bright Galaxies. Springer, New York
Dirsch B., Richtler T., Geisler D., Forte J. C., Bassino L., Gieren W., 2003, AJ, 125, 1908
Eggen O., Lynden Bell D., Sandage A. R., 1962, ApJ, 136, 748
Forbes D. A., Forte J. C., 2001, MNRAS, 322, 257
Forbes D. A., Brodie J. P., Grillmair C. J., 1997, AJ, 113, 1652

Forbes D. A. et al., 2004, MNRAS, 355, 608
Forbes D., Spitler L., Strader J., Romanowsky A., Brodie J., Foster C., 2011, MNRAS, 413, 2943
Forte J. C., Geisler D., Ostrov P. G., Piatti A. E., Gieren W., 2001, AJ, 121, 1992
Forte J. C., Faifer F., Geisler D., 2007, MNRAS, 382, 1947
Forte J. C., Vega I., Faifer F. R., 2009, MNRAS, 397, 1003
Fukazawa Y., Botoya-Nonesa J. G., Pu J., Ohto A., Kawano N., 2006, ApJ, 636, 698
Fukugita M., Shimasaku M., Ichikawa T., 1995, PASP, 107, 945
Fukugita M., Ichikawa T., Gunn J., Shimasaku M., Schneider D., 1996, AJ, 111, 1748
Geller M. J., Huchra J. P., 1983, ApJS, 52, 61
Gregg M. D., Ferguson H. C., Minniti D., Tanvir N., Catchpole R., 2004, AJ, 127, 1441
Harris W., 2009a, ApJ, 703, 939
Harris W., 2009b, ApJ, 699, 254
Harris W. E., Hanes D. A., 1985, ApJ, 291, 147
Harris G., Harris W., 2011, MNRAS, 410, 2347
Harris W. E., Whitmore B. C., Karakla D., Okon W., Baum W. A., Hanes D. A., Kavelaars J. J., 2006, ApJ, 636, 90
Harris W., Spitler L., Forbes D., Bailin J., 2010, MNRAS, 401, 1965
Hook I. M., Jorgensen I., Allington-Smith J. R., Davies R. L., Metcalfe N., Murowinski R. G., Crampton D., 2004, PASP, 116, 425
Jensen J., Tonry J., Barris B., Thompson R., Liu M., Rieke M., Ajhar E., Blakeslee J., 2003, ApJ, 583, 712
Jordán A., Peng E., Blakeslee J., Côté P., Eyheramendy S., Ferrarese L., Mei S., Tonry J., West M., 2009, ApJS, 180, 54
Kissler-Patig M., 2009, in Richtler T., Larsen S., eds, Globular Clusters – Guides to Galaxies, ESO Astrophysics Symposia. Springer, Berlin, p. 1
Kundu A., 2008, AJ, 136, 1013
Kundu A., Whitmore B. C., 1998, AJ, 116, 2841
Kundu A., Whitmore B. C., 2001, AJ, 121, 2950
Kundu A., Whitmore B., Sparks W., Macchetto F., Zepf S., Ashman K., 1999, ApJ, 513, 733
Kuntschner H., Ziegler B. L., Sharples R. M., Worthey G., Fricke K. J., 2002, A&A, 395, 761
Larsen S. S., Brodie J. P., Huchra J. P., Forbes D., Grillmair C. J., 2001, AJ, 121, 2974
Lauer T. R., Kormendy J., 1986, ApJ, 303, 1
Lee M. G., Park H. S., Kim E., Hwang H. S., Kim S. C., Geisler, 2008, ApJ, 682, 135
Liu C., Peng E., Jordán A., Ferrarese L., Blakeslee J., Côté P., Mei S., 2011, ApJ, 728, 116
MacDonald P. D. M., 2007, documentation and code at http://www.math.mcmaster.ca/peter/mix/mix.html, Department of Mathematics and Statistics, McMaster Univ., Ontario
Malin D. F., Carter D., 1980, Nat, 285, 643
Mendel J. T., Proctor R. N., Forbes D. A., 2007, MNRAS, 379, 1618
Metcalfe N., Shanks T., Campos A., McCracken H. J., Fong R., 2001, MNRAS, 323, 795
Mieske S., Hilker M., Infante L., Jordán A., 2006a, AJ, 131, 2442
Mieske S. et al., 2006b, ApJ, 653, 193
Mieske S. et al., 2008, A&A, 487, 921
Mulchaey J. S., Davis D. S., Mushotzky R. F., Burstein D., 2003, ApJS, 145, 39
Muratov A., Gnedin O., 2010, ApJ, 718, 1266
Norris M. A., Kannappan S. J., 2011, MNRAS, 414, 739
Norris M. A., Sharples R. M., Kuntschner H., 2006, MNRAS, 367, 815
Norris M. et al., 2008, MNRAS, 385, 40
Norris M. et al., 2011, MNRAS, submitted
Oser L., Ostriker J., Naab T., Johansson P., Burkert A., 2010, ApJ, 725, 2312
Ostrov P., Forte J. C., Geisler D., 1998, AJ, 116, 2854
O'Sullivan E., Forbes D., Ponman T., 2001, MNRAS, 328, 461
Peng E. W. et al., 2006, ApJ, 639, 95
Peng E. W. et al., 2009, ApJ, 703, 42
Pierce M. et al., 2006a, MNRAS, 366, 1253
Pierce M. et al., 2006b, MNRAS, 368, 325
Puzia T. H., Zepf S. E., Kissler-Patig M., Hilker M., Minniti D., Goudfrooij P., 2002, A&A, 391, 453
Puzia T. H. et al., 2004, A&A, 415, 123
Quinn P., 1984, ApJ, 279, 596
Randall S. W., Sarazin C. L., Irwin J. A., 2004, ApJ, 600, 729
Randall S. W., Sarazin C. L., Irwin J. A., 2006, ApJ, 636, 200
Revnivtsev M., Churazov E., Sazonov S., Forman W., Jones C., 2008, A&A, 490, 37
Rhode K., Zepf S., 2004, AJ, 127, 302
Robin A. C., Reylé C., Derrière S., Picaud S., 2003, A&AS, 409, 523
Sarazin C., Kundu A., Irwin J., Sivakoff G., Blanton E., Randall S., 2003, ApJ, 595, 743
Schlegel D. J., Finkbeiner D. P., Davis M., 1998, ApJ, 500, 525
Schweizer F., Seitzer P., 1992, AJ, 104, 1039
Searle L., Zinn R., 1978, ApJ, 205, 357
Sikkema G., Peletier R. F., Carter D., Valentijn E. A., Balcells M., 2006, A&A, 458, 53
Sil'chenko O. K., 2000, AJ, 120, 741
Sil'chenko O. K., Afanasiev V. L., Vlasyuk V. V., 1992, AZh, 69, 1121
Sinnott B., Hou A., Anderson R., Harris W., Woodley K., 2010, AJ, 140, 2101
Smith J. A. et al., 2002, AJ, 123, 2121
Spitler L., 2010, MNRAS, 406, 1125
Stetson P. B., 1987, PASP, 99, 191
Strader J., Smith G. H., 2008, AJ, 136, 1828
Strader J., Brodie, J. P., Spitler L., Beasley M., 2006, AJ, 132, 2333
Terlevich A., Forbes D., 2002, MNRAS, 330, 547
Thomas D., Maraston C., Korn A., 2004, MNRAS, 351, 19
Thomas D., Maraston C., Bender R., Mendes de Oliveira C., 2005, ApJ, 621, 673
Thomson R., Wright A., 1990, MNRAS, 247, 122
Tonry J. L., Dressler A., Blakeslee J. P., Ajhar E. A., Fletcher A. B., Luppino G. A., Metzger M. R., Moore C. B., 2001, ApJ, 546, 681
Tortora C., Napolitano N. R., Cardone V. F., Capaccioli M., Jetzer Ph., Molinaro R., 2010, MNRAS, 407, 144
Villegas D. et al., 2010, ApJ, 717, 603
Waters C., Zepf S., Lauer T., Baltz E., 2009, ApJ, 693, 463
Wehner E., Harris W., 2007, ApJ, 668, L35
Wehner E., Harris W., Whitmore B., Rothberg B., Woodley K., 2008, ApJ, 681, 1233
White R. E., Keel W. C., Conselice C. J., 2000, ApJ, 542, 761
Whitlock S., Forbes D. A., Beasley M. A., 2003, MNRAS, 345, 949
Zepf S. E., Geisler D., Ashman K. M., 1994, ApJ, 435, 117
Zepf S. E., Ashman K. M., Geisler D., 1995, ApJ, 443, 570

APPENDIX A: PHOTOMETRIC DATA

Table A1. Photometric catalogue of all the GC candidates in the five GCSs studied in this work. The magnitudes are from PSF fitting for the unresolved sources and from aperture photometry for the resolved sources. These magnitudes are extinction corrected, as indicated in the text. The complete photometry for GC candidates is available as Supporting Information with the on-line version of the article.

Object ID	RA	Dec.	x_{ccd}	y_{ccd}	g'_0	$\sigma_{g'}$	r'_0	$\sigma_{r'}$	i'_0	$\sigma_{i'}$
N4649GC2	12:43:33.74	11:34:02.5	1708.009	53.761	23.8009	0.023	23.1895	0.023	22.8163	0.024
N4649GC3	12:43:33.97	11:34:01.3	1685.015	62.249	22.7809	0.016	22.0355	0.008	21.6613	0.013
N4649GC4	12:43:29.01	11:34:01.2	2185.490	62.391	24.0299	0.013	23.5035	0.017	23.1393	0.025
N4649GC5	12:43:38.04	11:34:02.4	1273.952	55.273	23.7579	0.028	22.9325	0.016	22.5213	0.019
N4649GC6	12:43:41.82	11:34:02.4	892.493	55.250	23.6949	0.015	23.2035	0.015	22.9523	0.025
N4649GC7	12:43:41.24	11:34:03.2	950.987	50.004	23.9169	0.020	23.3875	0.019	23.3253	0.032
N4649GC8	12:43:34.64	11:33:58.9	1617.590	78.958	21.2469	0.008	20.7345	0.011	20.5343	0.013
N4649GC9	12:43:37.67	11:34:00.1	1310.816	70.643	22.5349	0.010	22.0455	0.017	21.7833	0.022
...	...	...	...	...	...	...	...	...	...	...

Table A2. The photometric data for all the UCD candidates in the five GCSs studied in this work. The magnitudes are from PSF fitting for the unresolved sources and from aperture photometry for the resolved sources. These magnitudes are extinction corrected, as indicated in the text. The complete photometry for UCD candidates is available as Supporting Information with the on-line version of the article.

Object ID	RA	Dec.	x_{ccd}	y_{ccd}	g'_0	$\sigma_{g'}$	r'_0	$\sigma_{r'}$	i'_0	$\sigma_{i'}$
N4649UCD1	12:43:41.23	11:30:48.3	952.676	1388.875	18.4779	0.003	17.8995	0.007	17.7183	0.006	...
...	...	...	...	...	...	...	...	...	...	...	...

SUPPORTING INFORMATION

Additional Supporting Information may be found in the on-line version of this article.

Table A1. Photometric catalogue of all the GC candidates in the five GCSs studied in this work.
Table A2. The photometric data for all the UCD candidates in the five GCSs studied in this work.

Please note: Wiley-Blackwell are not responsible for the content or functionality of any supporting materials supplied by the authors. Any queries (other than missing material) should be directed to the corresponding author for the article.

This paper has been typeset from a TEX/LATEX file prepared by the author.